

# 1 Curved atmospheric rivers and their moisture remnants: a new 2 detection tool for Antarctica

3 Victoire Buffet<sup>1,2</sup>, Vincent Favier<sup>1</sup>, Benjamin Pohl<sup>2</sup>, Jonathan D. Wille<sup>1</sup>

4 <sup>1</sup>Université Grenoble Alpes/CNRS/IRD/G-INP, IGE, Grenoble, 38000, France

5 <sup>2</sup>Biogéosciences, UMR6282 CNRS / Université Bourgogne Europe, Dijon, 21000, France

6 *Correspondence to:* Victoire Buffet (victoire.buffet@univ-grenoble-alpes.fr)

7 **Abstract.** Atmospheric rivers (ARs) represent the main intrusions of moisture and heat into Antarctica, exerting a major  
8 influence on the continent's surface mass balance. Yet, due to geometric and directional constraints, existing detection  
9 algorithms often fail to track their evolution inland after landfall or in regions where abrupt directional changes occur. We  
10 introduce DARK (Detecting ARs using their Kurvature), a new Antarctic AR detection framework designed to overcome these  
11 limitations. DARK applies a strict 98th-percentile threshold to total integrated vapor transport and computes AR length along  
12 the curved axis to evaluate the 2000-km AR criterion. This enables the continuous detection of ARs with complex geometries,  
13 including those that curve, overturn, or extend across the South Pole. An additional AR-children module identifies smaller but  
14 still intense moisture remnants that detach from parent ARs after landfall yet continue to transport vapor and heat inland. The  
15 resulting climatology shows that DARK ARs account for about 18 % of total Antarctic precipitation and are linked to roughly  
16 half of top 1 % daily precipitation anomalies, 60 % of top 1 % daily maximum temperature anomalies, and 80 % of compound  
17 warm-and-wet events. DARK provides a more detailed assessment of AR-related precipitation and temperature impacts in the  
18 South Pole region. Despite slightly higher occurrence, risk ratio analysis shows that DARK ARs more effectively capture the  
19 most intense events than earlier Antarctic schemes. Including AR-children further strengthens these associations, especially  
20 over Victoria Land, where they contribute to about one third of AR-related precipitation.

21  
22  
23  
24  
25  
26  
27  
28  
29

30 **Plain Language Summary.** Atmospheric rivers (ARs) are long, narrow bands of air that carry large amounts of moisture and  
31 heat from the lower latitudes into Antarctica, where they trigger snowfall, surface melt, and extreme temperature events.  
32 Existing tools to detect these features often miss them when they arrive at the coast in unusual directions or continue moving  
33 inland after landfall. We developed a new detection method, called DARK, that can identify atmospheric rivers regardless of  
34 their shape or direction, including those that curve or cross the South Pole. DARK also tracks smaller moisture remnants,  
35 called AR-children, that split off from the main system after it reaches the continent but continue to bring moisture inland. Our  
36 results show that atmospheric rivers detected by DARK are responsible for about 18 % of Antarctic snowfall and are associated  
37 with half of the top 1 % precipitation anomaly days, 60 % of the top 1 % warm anomaly days, and 80 % of days with  
38 simultaneous top 1 % warm and precipitation anomalies. AR-children make additional contributions, particularly in Victoria  
39 Land. This new framework provides a more complete picture of how atmospheric rivers shape the weather and mass balance  
40 of the Antarctic Ice Sheet.~~Atmospheric rivers (ARs) are long, narrow corridors of air that transport large amounts of water~~  
41 ~~vapor and heat from lower latitudes into Antarctica. These events play a major role in shaping Antarctic weather and the ice~~  
42 ~~sheet's mass balance, but many current detection methods struggle to track them accurately as they move inland. We developed~~  
43 ~~a new method, called DARK (Detecting Atmospheric Rivers using their Kurvature), that can identify and follow atmospheric~~  
44 ~~rivers with complex shapes, including those that curve or cross the South Pole. The method also detects smaller features, called~~  
45 ~~"AR-children", which break away from larger systems but continue to carry moisture and warmth inland. Our results show~~  
46 ~~that ARs detected by DARK contribute to about 18 % of all Antarctic precipitation and are linked to many extreme events,~~  
47 ~~including half of the most intense daily precipitation, 60 % of high temperature days, and 80 % of events that are both warm~~  
48 ~~and wet. Including the smaller AR children further strengthens these associations, particularly in regions such as Victoria~~  
49 ~~Land. Although part of this increase reflects the larger number of detected ARs, risk ratio analysis shows that DARK ARs are~~  
50 ~~equally or more effective at capturing these intense anomalies. This framework provides a more complete understanding of~~  
51 ~~AR-driven processes that influence the Antarctic Ice Sheet.~~

52  
53  
54 **Keywords :** Atmospheric rivers – Antarctica – Precipitation – Detection tool – Methodology

## 55 **1 Introduction**

56 Atmospheric rivers (ARs) are long, narrow filaments of enhanced horizontal water vapor transport that are an essential  
57 component of the global hydrological cycle and particularly play a central role in the Antarctic surface mass balance (e.g. Zhu  
58 and Newell, 1998; Wille et al., 2025). ARs contribute positively to the Antarctic Ice Sheet (AIS) mass balance through  
59 enhanced snowfall (Turner et al., 2019; Wille et al., 2021; MacLennan et al., 2022), but they can also induce surface melt and  
60 promote ice-shelf instability when transporting warm, moist air masses inland (Gorodetskaya et al., 2014; Adusumilli et al.,

61 2021; Wille et al., 2019; Wille et al., 2022). Given their dual role, robust detection of ARs is essential for quantifying their  
62 frequency and impacts.

63  
64 Many AR detection tools (ARDTs) have been developed for different purposes and regions (Collow et al., 2022), but only a  
65 few are tailored to polar environments (Wille et al., 2021; Gorodetskaya et al., 2014; Mattingly et al., 2018; Wille et al., 2025).  
66 At the global scale, the most widely used scheme remains that of Guan and Waliser (2015), recently updated in Guan and  
67 Waliser (2024). It employs seasonally and spatially varying vertically integrated water vapor transport (IVT) thresholds (85th  
68 percentile), which provide broad applicability and robust intercomparison across reanalyses (Collow et al., 2022). The method  
69 also applies a set of geometric and directional filters, including a minimum feature length of about 2000 km, a length-to-width  
70 ratio requirement to ensure narrow filamentary structures, and directional coherence criteria that retain only elongated,  
71 dynamically consistent moisture transport features. In its latest version (Guan and Waliser, 2024; hereafter G&W v4), several  
72 refinements were introduced, including a revised treatment of directional coherence, improved handling of zonally oriented  
73 ARs in the extratropics, and a polar refinement based on a hemispheric IVT threshold, defined from the area-weighted spatial  
74 5th percentile of local IVT thresholds. This replaces the previously fixed 100 kg m<sup>-1</sup>s<sup>-1</sup> minimum and allows ARs to extend  
75 farther inland in polar regions. Despite these advances, limitations remain over Antarctica. Because the threshold is based on  
76 hemispheric IVT climatology, its effective local percentile varies strongly across the continent. It corresponds to relatively low  
77 local percentiles in West Antarctica and coastal regions, favoring numerous AR detections, but to very high percentiles over  
78 the cold, dry East Antarctic interior, sometimes exceeding the 99th percentile, which prevents inland detections. Consequently,  
79 AR occurrence remains spatially heterogeneous, with frequent detections along the coast and in West Antarctica but few over  
80 much of the East Antarctic Ice Sheet.  
81 ~~also includes a minimum feature length of 2000 km (Zhu and Newell, 1998) and additional directional and coherence~~  
82 ~~constraints, requiring a minimum poleward IVT component and a coherent IVT direction. However, the Guan and Waliser~~  
83 ~~framework shows limited skill over Antarctica, as its lower IVT percentile threshold tends to identify extensive zonal moisture~~  
84 ~~bands that circulate around the ice sheet without significant inland penetration.~~

85  
86 For Antarctica, the most widely used polar-specific ARDT is that of Wille et al. (2021), which includes two variants of the  
87 same method applied to different input variables: the meridional component of IVT (vIVT, hereafter Wille vIVT) and vertically  
88 integrated water vapor (IWV, hereafter Wille IWV). Among these, the vIVT-based version is the most commonly used. It  
89 applies a monthly, locally defined 98th-percentile threshold on vIVT, combined with a 20° meridional extent criterion, to  
90 identify the strongest southward moisture intrusions linking the lower latitudes to the Antarctic continent. This design is  
91 physically consistent with the dynamics of extreme Antarctic precipitation, as intense snowfall events are generally associated  
92 with above-average IVT directed southward and approximately perpendicular to the coast (Wille et al., 2021). Consequently,  
93 the Wille vIVT scheme effectively isolates the ARs that have been linked to intense precipitation (Wille et al., 2021; Maclennan  
94 et al., 2022), surface melt (Wille et al., 2019, Gorodetskaya et al., 2023), firn depletion, large iceberg calving events, and ice-

95 shelf destabilization (Wille et al., 2022). Thus, this ARDT has become the reference framework for polar AR studies (Wille et  
96 al., 2025).

97  
98 However, the Wille et al. (2021) framework, while robust, does not capture the full range of intense moisture transport features  
99 relevant to Antarctica. While weaker or more diffuse intrusions are rightly excluded by design, some long, narrow, and intense  
100 filaments of water vapor transport, dynamically consistent with the physical definition of ARs (American Meteorological  
101 Society, 2022), remain undetected. This underdetection arises from methodological constraints related to the orientation,  
102 coherence, and geometric requirements of the detection scheme.

103  
104 First, the use of vIVT in the Wille vIVT scheme introduces a discontinuity at the South Pole. When an AR crosses the pole,  
105 the sign of vIVT reverses from poleward to equatorward, preventing its identification. This discontinuity also breaks the  
106 continuity of the feature's axis, preventing it from satisfying the minimum length criterion ( $20^\circ$  meridional extent) at the  
107 highest latitudes. This issue does not affect the Wille IWV scheme, which does not consider the meridional wind; however,  
108 Wille et al. (2021) restricted their detection domain to  $85^\circ$  S (Fig. 1b) to avoid this singularity, in both vIVT and IWV schemes,  
109 to maintain consistency of AR climatologies between both algorithms. While this boundary had little impact on coastal AR  
110 landfalls and when tracking their progression inland, it introduces a progressive detection bias toward lower latitudes, up to  
111 around  $65^\circ$  S, as a result of the  $20^\circ$  meridional-extent requirement.

112  
113 Second, focusing on “moisture transport axes,” a term introduced to unify ARs, tropical moisture exports, and warm moist  
114 intrusions; Spensberger et al. (2025) note that one third of those axes exhibit an equatorward component. This behavior likely  
115 reflects synoptic-scale processes such as frontal occlusion and the curvature of moisture pathways within mature cyclones, as  
116 well as the modulation of moisture transport by quasi-stationary large-scale circulation features and topographic forcing. As  
117 these systems move poleward and their associated ARs approach the Antarctic coast, they interact with the prevailing near-  
118 surface easterlies and the steep topography of the ice sheet margin. These interactions often cause the moisture plumes to curve  
119 or tilt at landfall, deviating from a purely meridional orientation. Approximately 20% of “moisture transport axes” south of  
120  $70^\circ$  S display such equatorward curvature (Spensberger et al., 2025). This behavior is particularly common in the Ross Sea  
121 and Weddell Sea regions (see Fig. 1a for geographic regions referenced in this study), where synoptic and orographic effects  
122 jointly steer moisture fluxes away from the meridional direction. In these cases, vIVT decreases and reverses sign as the AR  
123 curves equatorward, leading to a loss of detection at and beyond the inflection point. Although this specific limitation does not  
124 affect the Wille IWV scheme, it remains constrained by the  $20^\circ$  meridional-extent criterion, which also excludes long, curved,  
125 or overturning ARs that are dynamically consistent with AR characteristics but have limited meridional span due to their  
126 complex geometry. This limitation is not unique to the Wille vIVT and IWV frameworks. Global AR detection schemes such  
127 as G&W v4 also apply directional-coherence constraints that may limit the detection of ARs with strongly curved or reversing  
128 geometries, though their primary limitation over Antarctica relates to the effective IVT threshold rather than directionality, as

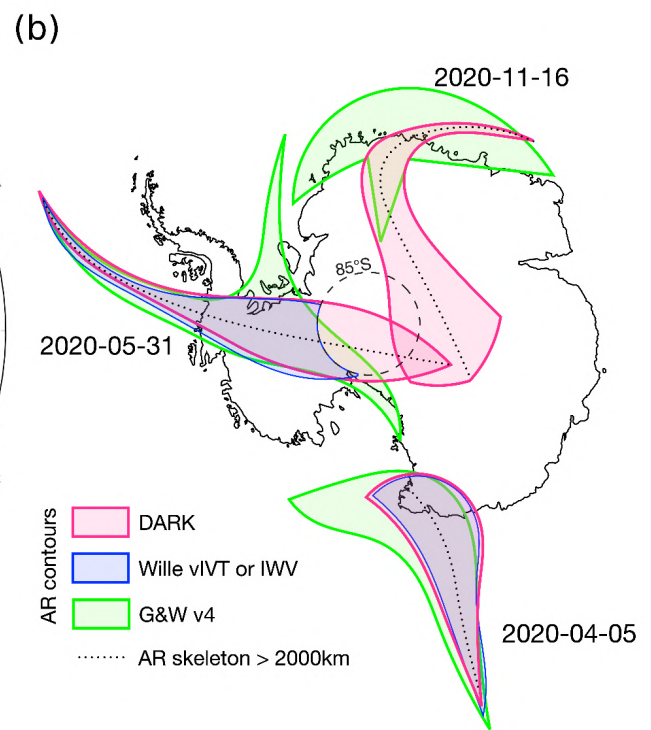
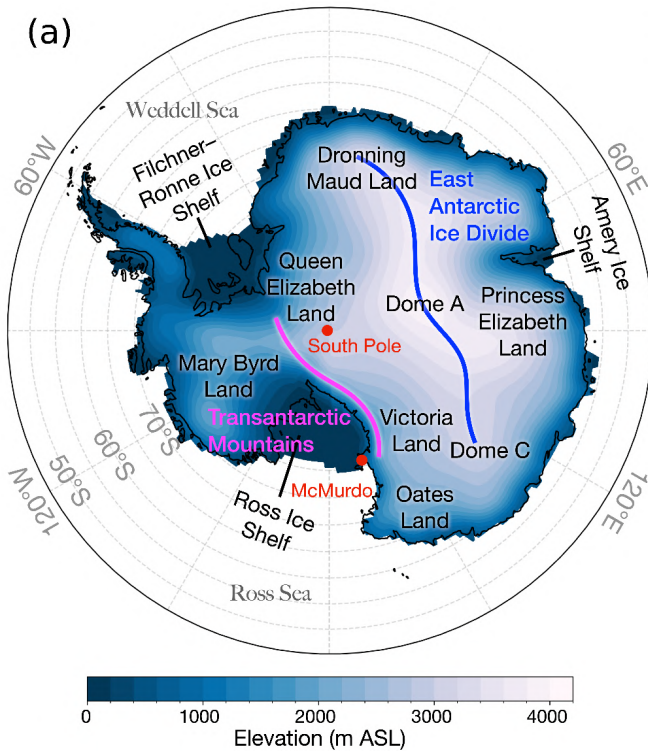
129 ~~further discussed in Sect. 3. This limitation is not unique to the Wille et al. (2021) framework, as global AR detection schemes~~  
130 ~~such as Guan and Waliser (2015) also omit such events because their directional coherence criteria preclude the detection of~~  
131 ~~curved or horseshoe-shaped ARs.~~

132  
133 Another limitation of existing detection approaches concerns the evolution of ARs after they reach the Antarctic continent.  
134 As they make landfall, they often diverge and lose their narrow filamentary geometry due to condensation, latent heat release,  
135 and the spreading of moisture fluxes within occluding or decaying frontal systems (Dacre and Clark, 2025). Although this  
136 morphological transition causes them to fall outside the geometric criteria of standard AR detection methods, these features  
137 frequently remain highly moisture-laden and continue to drive precipitation, cloud formation, and surface melt inland. To  
138 capture the continuation of AR influence, identifying and tracking such post-landfall remnants would be relevant but has not  
139 yet been proposed. This would allow the monitoring of structures representing the inland evolution of decaying but still active  
140 AR-provided moisture remnants. Accounting for these structures would be essential for quantifying the sustained hydrological  
141 and thermodynamic effects of ARs on the Antarctic surface mass balance, while extending the study of the Antarctic AR life  
142 cycle to its terminus (Wille et al., 2024).

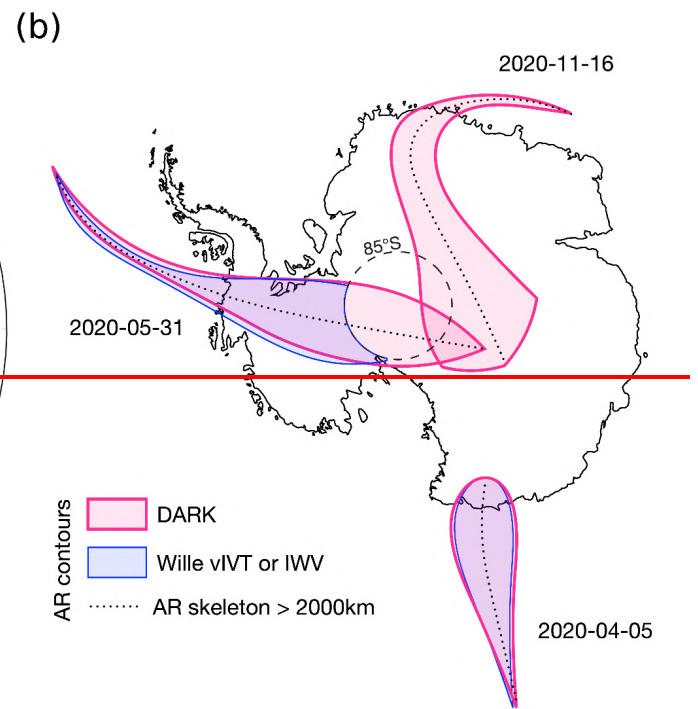
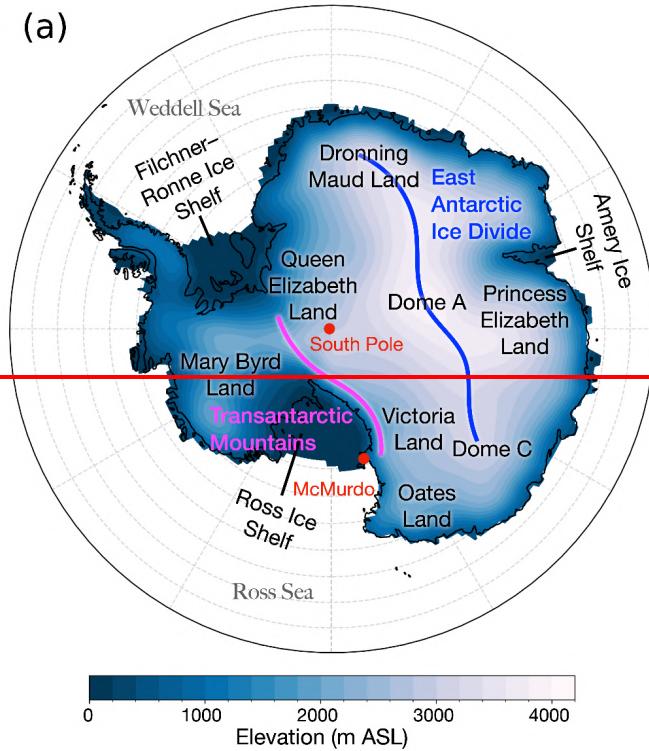
143 To address these limitations, we develop a new Antarctic ARDT called DARK (Detecting ARs using their Kurvature), that  
144 builds upon the intensity-based framework of Wille et al. (2021) while removing directional constraints that limit the  
145 identification of curved or equatorward-turning ARs (like the AR making landfall on 2020-11-16, in Dronning Maud Land,  
146 Fig. 1b). The method applies a 98th-percentile threshold on total integrated vapor transport (IVT), computed using a 15-day  
147 rolling window to capture temporal variability and regional seasonality. Features smaller than 200,000 km<sup>2</sup> are removed prior  
148 to classification. ARs are then defined as contiguous structures exceeding the IVT threshold with a total length of at least 2000  
149 km, approximately equivalent to the 20° meridional extent criterion of Wille et al. (2021) (Fig. 1b), but regardless of their  
150 orientation or directional coherence. In addition, we introduce an add-on to identify and track post-landfall moisture remnants  
151 with IVT above the local 98th-percentile, with an area exceeding 20,000 km<sup>2</sup>, which evolve from previously detected ARs but  
152 no longer meet the geometric length criterion, hereafter referred to as AR-children. This study aims to illustrate that our  
153 framework provides a more complete and physically consistent view of AR-driven moisture transport and its influence on  
154 Antarctic precipitation and near-surface temperature variability, with implications for surface melt and ice-shelf stability.

155 We apply this framework to a multi-decadal ERA5 reanalysis (1979–2023) to produce the first comprehensive assessment of  
156 Antarctic ARs detected by DARK that explicitly includes curved ARs (hereafter DARK ARs) and their post-landfall AR-  
157 children. The analysis quantifies their contribution to Antarctic precipitation, as well as to precipitation, temperature, and  
158 compound ~~anomalies and~~ extreme anomalies. It further characterizes the magnitude and orientation of IVT and presents  
159 representative case studies illustrating their synoptic evolution. Throughout, DARK is compared against the Wille vIVT, Wille  
160 IWV, and G&W v4 catalogues to contextualize its added value. This framework aims to fill key observational and

161 methodological gaps left by existing ARDTs, providing a more comprehensive representation of Antarctic ARs and their  
162 impacts on the AIS.



163



164

165 Figure 1. (a) Map of the Antarctic Ice Sheet showing surface elevation (m a.s.l.) and key geographic regions discussed in the  
166 text. (b) Conceptual schematic illustrating detection differences between the DARK\_ ~~and~~ Wille AR and G&W v4 frameworks  
167 during three arbitrary yet representative landfall events.

## 168 **2 Data and methodology**

### 169 **2.1 Data**

170 We use the ERA5 reanalysis produced by the European Centre for Medium-Range Weather Forecasts (ECMWF; Hersbach et  
171 al., 2020) for the period 1979–2023, at a horizontal resolution of  $0.25^\circ \times 0.25^\circ$ . Atmospheric rivers are detected at 6-hourly  
172 intervals using the eastward ( $uIVT$ ) and northward ( $vIVT$ ) components of integrated vapor transport (IVT). Diagnostic  
173 variables, including wind and geopotential height at 500 hPa, are analyzed at the same 6-hourly timestep.  
174 Surface diagnostics are evaluated at daily resolution: total precipitation is aggregated to daily sums, and 2 m air temperature  
175 is used to derive daily maximum values.

176 For intercomparison, the Wille et al. (2021) Antarctic AR detection schemes based on integrated water vapor (IWV) and  
177 meridional IVT ( $vIVT$ ) were recomputed at 6-hourly intervals. To ensure spatial consistency with the new DARK framework,  
178 both Wille schemes were extended northward to  $15^\circ$  S while retaining their original southern boundary at  $85^\circ$  S. This  
179 adjustment provides uniform temporal and spatial coverage across methods, enabling a direct comparison of AR frequency,  
180 geometry, and associated surface impacts over the 1979–2023 period.

181 We additionally use the tARget version 4 AR catalog (Guan and Waliser, 2024; hereafter referred to as G&W v4), generated  
182 from ERA5 for 1940–2023. Only the 1979–2023 period is retained to match the analysis window used throughout this study.

### 184 **2.2 DARK AR Detection Algorithm**

185  
186 At each 6-hourly time step, the DARK framework is applied over the  $15^\circ$  S– $90^\circ$  S domain. The magnitude of IVT is computed  
187 from its zonal and meridional components as

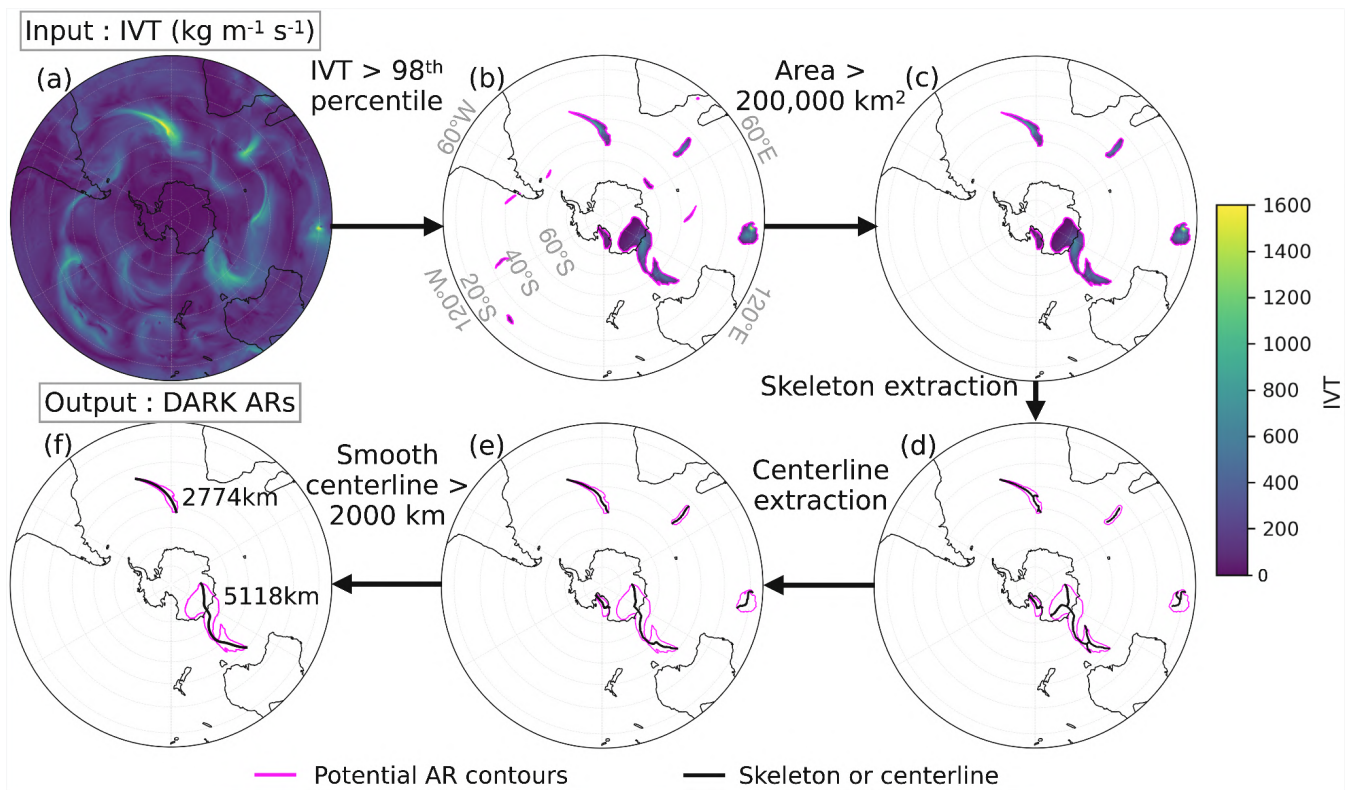
$$188 \quad IVT = \sqrt{uIVT^2 + vIVT^2} \quad (1)$$

189 where  $uIVT$  and  $vIVT$  are the zonal and meridional components of IVT from ERA5.

190 A rolling 15-day 98th-percentile threshold of IVT is calculated for each grid point and day of year using all available years  
191 (1979–2023). Grid cells exceeding this threshold are identified at each 6-hourly time step and grouped into contiguous features  
192 using a connectivity criterion that links all directly adjacent or diagonally touching cells (Fig. 2a). Objects smaller than 200,000

km<sup>2</sup> are removed (consistent with the typical spatial scale of ARs, which are generally hundreds of kilometres wide and at least 2,000 km long) before centerline computation to avoid processing small, isolated exceedances that are not representative of large-scale moisture transport and for which centerline estimation is computationally expensive and prone to numerical error (Fig. 2b).

The remaining features are processed to extract a reduced to a one-pixel wide skeleton using a morphological thinning algorithm. This skeleton is then converted into a graph representation from which all endpoint to endpoint paths are extracted. The longest and most directionally consistent path, determined using principal component analysis, is selected as the primary centerline. The path is extended to the object's edge, smoothed using a B-spline interpolation, and resampled to 200 evenly spaced points. The total AR length is finally computed as the geodesic distance along this smoothed centerline (Fig. 2d,e); while accounting for longitudinal wrapping. An object is classified as an AR if the geodesic length of this centerline equals or exceeds its total centerline length is equal to or greater than 2000 km, consistent with the typical length scale used in established AR detection frameworks (Fig. 2f; e.g., Guan and Waliser, 2015; Guan and Waliser, 2024; Wille et al., 2021; Skinner et al., 2020; Gorodetskaya et al., 2014). This procedure yields a binary AR mask indicating the presence or absence of an AR at each grid point and time step.



210 [Figure 2. Schematic overview of the DARK detection workflow applied to a single 6-hourly ERA5 time step. \(a\) Total IVT](#)  
211 [field used as input. \(b\) Grid cells exceeding the local 98th-percentile threshold. \(c\) Objects with an area exceeding 200,000](#)  
212 [km<sup>2</sup> retained. \(d\) Skeleton extracted from each remaining object. \(e\) Smoothed centerline derived from the skeleton. \(f\) Final](#)  
213 [DARK AR classification: objects whose centerline geodesic length equals or exceeds 2000 km are retained, with their](#)  
214 [centerline length indicated in km. Magenta contours show the potential \(b–e\) or final \(f\) AR object boundaries and black](#)  
215 [lines show the skeleton \(d\), centerline \(e\) or smoothed centerline \(f\).](#)

### 217 **2.3 Optional AR-children add-on**

218  
219 The AR-children add-on is an optional extension of the main detection algorithm. It builds upon the AR catalog described  
220 above to identify post-landfall moisture structures that remain intense after the parent AR loses spatial coherence. Accordingly,  
221 two catalogs are provided: one including only DARK ARs and another combining DARK ARs with their AR-children, with  
222 accompanying binary and classification variables (see Data Availability). At each time step, regions where IVT exceeds the  
223 98th-percentile threshold are labeled as contiguous features using a connectivity criterion that links all directly adjacent or  
224 diagonally touching grid cells. Temporal continuity is established through spatial overlap between consecutive time steps,  
225 ensuring consistent tracking of moisture structures while maintaining computational efficiency. A feature is classified as an  
226 AR-child when it previously overlaps with a detected parent AR and subsequently detaches from it while being in contact  
227 with, or located over, the Antarctic continent. A minimum area of 20,000 km<sup>2</sup> is imposed to exclude small structures. This  
228 approach ensures both physical and temporal consistency while remaining computationally efficient for multi-decadal,  
229 hemispheric reanalysis datasets.

230 [The AR-children module requires approximately 9h of CPU time and ~17 GB of memory for the full 1979–2023 climatology,](#)  
231 [compared to 1h and ~8 GB for the core DARK algorithm \(see Code and Data Availability section\).](#)

### 233 **2.4 Attribution of events to ARs**

234  
235 To attribute surface impacts to ARs (or AR-children), we identify precipitation and temperature events ~~temporally~~-associated  
236 with AR occurrence [at each grid cell](#). Because AR-related precipitation and temperature anomalies can persist beyond the  
237 period when a given grid cell is directly affected by an AR, the attribution window is extended to include adjacent days,  
238 depending on the variable.

239  
240 For precipitation, AR-related events are defined as those occurring on the day of AR landfall ( $D_0$ ) and the following day ( $D_{+1}$ ),  
241 following Wille et al. (2021) and Maclennan et al. (2022). We use here a daily timescale for computing efficiency and to avoid  
242 multiple detections of single extreme events due to serial correlation at sub-daily timescales. This extension accounts for  
243 residual precipitation that continues after the main AR plume loses coherence or moves inland.

244

245 For temperature, AR-related events are considered on the day before ( $D_{-1}$ ), the day of ( $D_0$ ), and the day after ( $D_{+1}$ ) AR landfall.  
246 This accounts for both preconditioning (e.g., warm advection ahead of the AR) and lagged warming due to persistent cloud  
247 cover, latent heat release, or surface melt following AR passage.

248 For precipitation, daily totals are compared to the mean daily climatology for each calendar day (1979–2023), while for 2 m  
249 air temperature, daily maxima are compared with the corresponding daily-maximum climatology. In both cases, the anomaly  
250 represents the deviation from the daily mean climatological value at each grid point.

251 Extreme events are defined as days when these anomalies exceed the 99th percentile of their respective daily anomaly  
252 distributions, computed independently at each grid point. Compound events, defined as the co-occurrence of extreme  
253 precipitation and temperature anomalies, are identified when an extreme precipitation day coincides with or occurs within  $\pm 1$   
254 day of an extreme temperature anomaly. This temporal window ensures that temporally overlapping or closely spaced extremes  
255 are captured within a single compound-event framework. This approach allows both direct and short-lagged compound  
256 extremes associated with ARs to be included in the analysis.

## 257 **2.5 Characterisation of AR moisture transport directionality**

258 To characterise the directionality of moisture transport during AR events, we analyse the ERA5 IVT components ( $uIVT$  and  
259  $vIVT$ ; eastward and northward respectively) at each grid cell and 6-hourly time step flagged as an AR over the 1979–2023  
260 period. Three metrics are computed for each grid cell. First, the fraction of AR time steps where meridional flow dominates  
261 (i.e.  $|vIVT| > |uIVT|$ ) is computed as a percentage of all AR time steps at that grid cell; the complementary fraction corresponds  
262 to zonal-dominant flow ( $|uIVT| > |vIVT|$ ). Second and third, the fraction of AR time steps with eastward ( $uIVT > 0$ ) and  
263 northward ( $vIVT > 0$ ) IVT are computed likewise.

## 264 **2.6 Risk Ratio**

265

266 Because extending the attribution window naturally increases the number of AR-associated events, we quantify their statistical  
267 relevance using risk ratios (RR; [Katz et al., 1978](#); [Scholtz and Lora, 2024](#)). This ensures that higher counts reflect genuine  
268 physical associations rather than the effect of broader temporal inclusion. RR are computed as the ratio between the probability  
269 of an extreme event during AR conditions (Eq. 2) and the probability during non-AR conditions (Eq. 3).

270 For each grid point, the conditional probabilities are defined as:

271 
$$P(E | AR) = \frac{N_{E,AR}}{N_{AR}} \quad (2)$$

$$P(E | \neg AR) = \frac{N_{E,\neg AR}}{N_{\neg AR}} \quad (3)$$

where  $N_{E,AR}$  is the number of days with both an AR and an extreme event (considering the temporal extension defined in Sect. 2.65),  $N_{AR}$  is the total number of AR days (including the temporal extensions defined in Sect. 2.65),  $N_{E,\neg AR}$  is the number of extreme events without an AR, and  $N_{\neg AR}$  the number of non-AR days. RR is then expressed as:

$$RR = \frac{P(E|AR)}{P(E|\neg AR)} \quad (4)$$

Values of  $RR > 1$  indicate that extreme events are more likely under AR conditions. For example, a value of  $RR = 2$  implies that extreme events are twice as likely to occur during AR conditions compared to non-AR conditions. This metric accounts for the frequency of AR occurrence, ensuring that results reflect the relative enhancement of extremes rather than the prevalence of ARs themselves.

## 2.76 Statistical significance

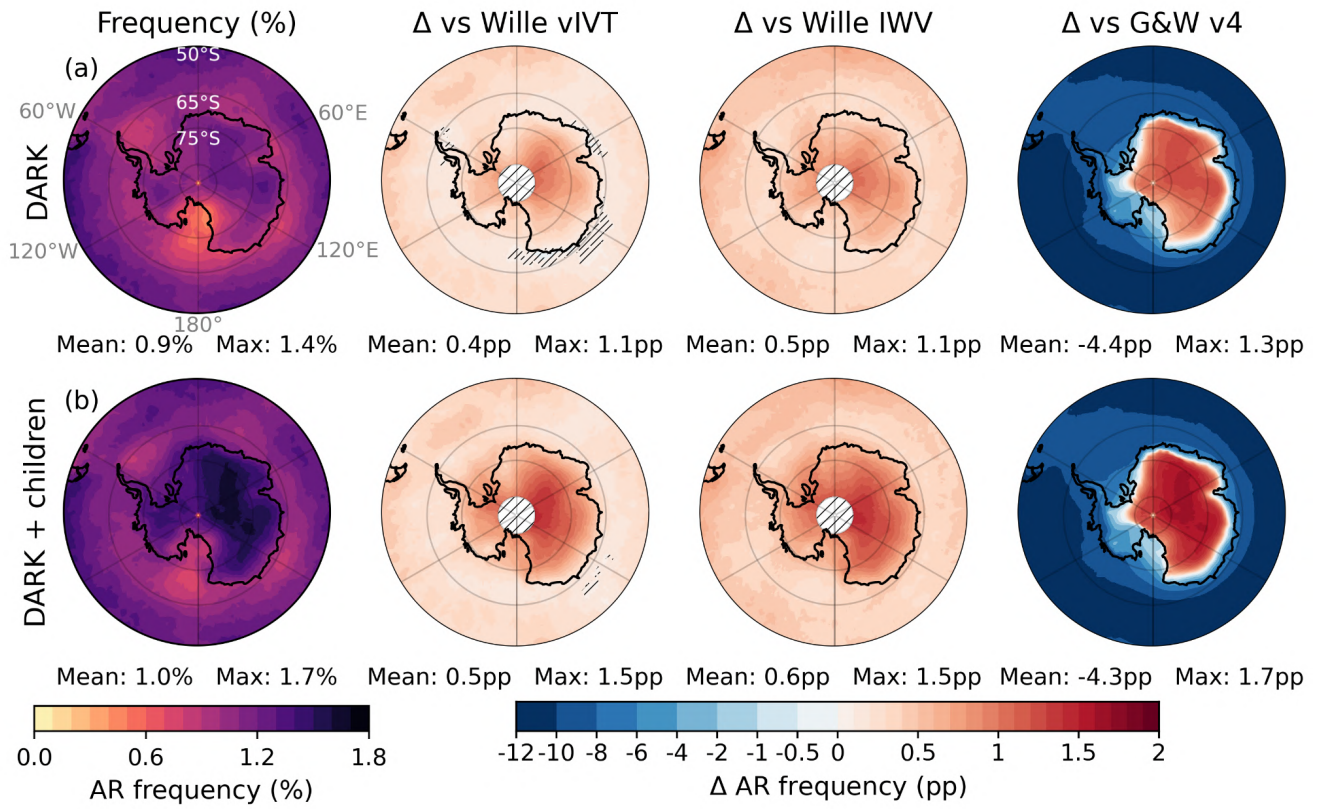
Differences in AR occurrence between schemes were evaluated using a two sample test of equality of proportions at each grid point. For the share of precipitation attributable to ARs, as well as for extreme precipitation, temperature, and compound events, significance was assessed using the same bootstrap framework: AR dates (including their variable-dependent temporal extensions) were kept fixed, while entire precipitation or temperature years were permuted without replacement, preserving their autocorrelation and seasonality but breaking their co-occurrence with ARs. The observed AR-associated fraction (or the difference between detection schemes) was compared against 1000 bootstrap realizations, and values were considered significant when they lay outside the corresponding 95 % bootstrap confidence interval.

The statistical significance of the RRs was assessed following the log-normal approximation method of Katz et al. (1978), because the distribution of the risk ratio is asymmetric while its logarithm is approximately normally distributed, allowing reliable confidence intervals to be derived using standard normal theory. To handle zero count cases, we applied the Haldane–Anscombe correction (Haldane, 1940; Anscombe, 1956) by adding 0.5 to both co-occurrence counts and 1 to the total-event denominators. A 95 % confidence interval was computed on the log-transformed RR and then exponentiated back to the RR scale. Grid cells were considered significant when the confidence interval excluded 1; otherwise, they were masked as non-significant.

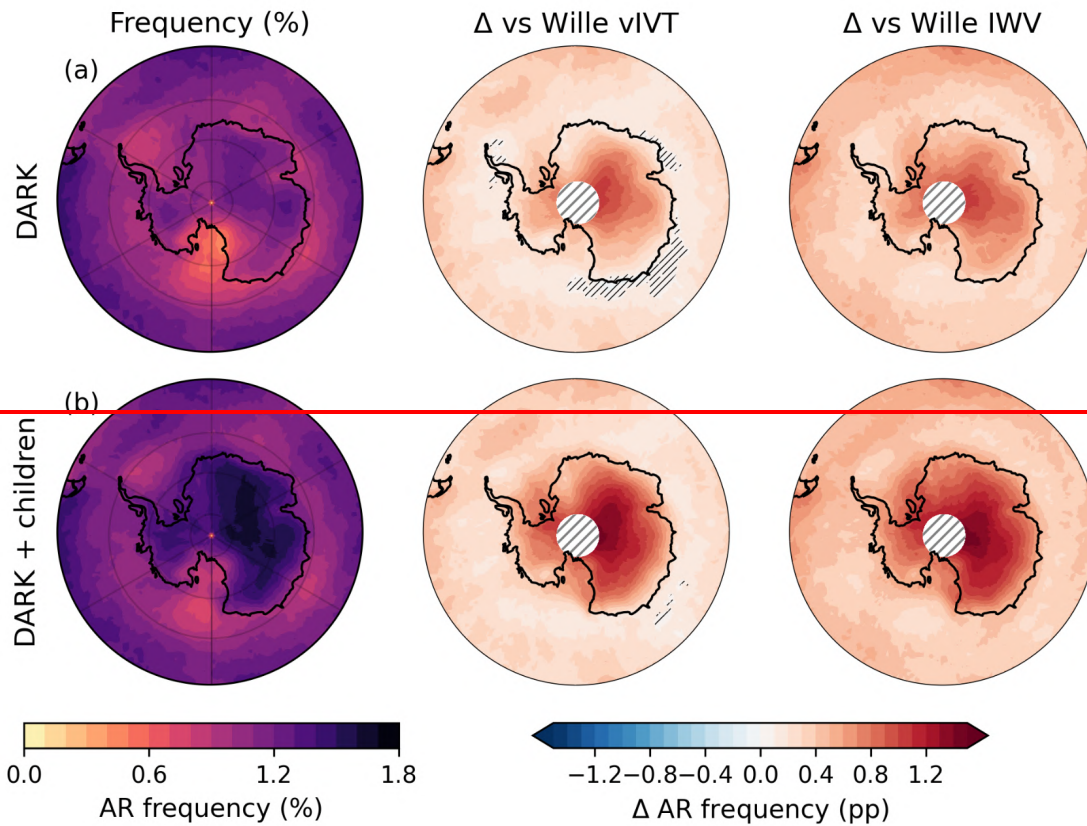
301 **3.1 Frequency of DARK ARs and AR-children**

302 DARK ARs exhibit their highest occurrence within the midlatitude storm-track regions ( $\sim 50^\circ\text{S}$ , Fig. 3Fig-2a; Chemke et al.,  
303 2022) (Chang et al., 2002; Wirth et al., 2018), with maxima during austral winter (see Fig. S1). The lowest frequencies occur  
304 over the Ross Sea sector, where the minimum is most pronounced in winter. The spatial distribution closely matches that of  
305 Wille vIVT and Wille IWV schemes, although DARK ARs yields higher overall frequencies, particularly over the AIS. Over  
306 South of the East Antarctic Ice Divide (EAID, Fig. 1a), occurrence is up to 1.2 percentage points (pp) higher than in Wille  
307 vIVT and IWV, while along the East Antarctic coast the difference remains small ( $\approx 0.3$  pp), indicating that the total frequency  
308 of AR landfalls along the Antarctic coastline remains roughly unchanged between the Wille and DARK schemes. By  
309 construction, AR-children occur exclusively over the continent and its coastal margins, with mean frequencies up to 0.3 %  
310 along the coast and local maxima of 0.6 % near McMurdo and farther inland over the plateau (Fig. S2a), bringing the total  
311 frequency of DARK ARs and their AR-children at 1.5 % across most of the AIS (Fig. 3Fig-2b).

312 The G&W v4 scheme exhibits a strikingly different spatial distribution of AR occurrence from both DARK and the Wille  
313 schemes. On average, G&W v4 detects 4.4 pp more AR occurrence than DARK across the Antarctic continent, but this average  
314 conceals an extreme spatial heterogeneity. Along the coast of West Antarctica, the Antarctic Peninsula, and the broader AIS  
315 coastline, G&W v4 exceeds DARK by up to 10 pp, while inland, south of the East Antarctic Ice Divide, DARK detects up to  
316 1.3 pp more than G&W v4 (Fig. 3Fig-2a). This sharp gradient is further illustrated in Fig. S3: G&W v4 detects more than  
317 2000 AR days at the coastline but fewer than 10 South of the EAID over the full 1979–2023 period, compared to around 400  
318 for DARK and around 300 for the Wille schemes. This sharp coastal-to-inland gradient reflects a fundamental limitation of  
319 the G&W v4 hemispheric threshold for capturing the full lifecycle of Antarctic ARs, and results in detection frequencies that  
320 are either far in excess of or far below those of DARK and the Wille schemes across most of the continent, with only a narrow  
321 transitional zone where they are broadly comparable. While G&W v4 effectively detects the most intense moisture intrusions  
322 at the coast, where IVT is highest, its effective threshold of  $46.8 \text{ kg m}^{-1}\text{s}^{-1}$  in January and  $39.4 \text{ kg m}^{-1}\text{s}^{-1}$  in July (Guan and  
323 Waliser, 2024) prevents detection of ARs as they penetrate inland and progressively lose intensity. As shown in Fig. S4, mean  
324 AR IVT values for DARK and the Wille schemes decrease to  $10 \text{ kg m}^{-1} \text{ s}^{-1}$  or below south of the EAID, well below the G&W  
325 v4 effective threshold, and G&W v4 records no detections (Fig. S3) at all over some interior regions such as Dome A and the  
326 area surrounding the South Pole. This suggests that G&W v4 captures the arrival of the most intense ARs at the Antarctic  
327 margin, but is not designed to monitor their inland penetration and associated surface impacts on the ice sheet.



328



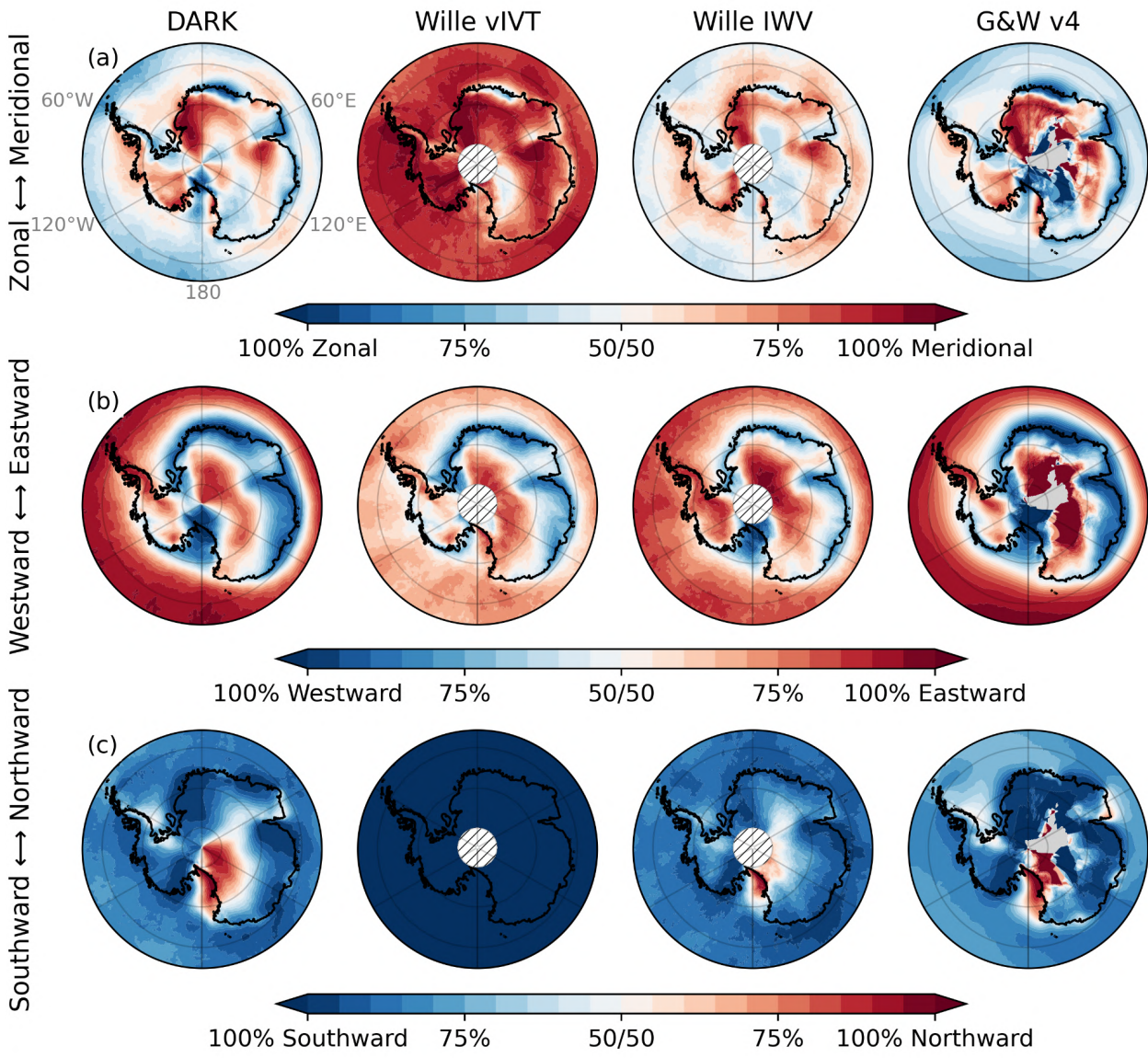
329  
 330 Figure 32. Frequency of DARK atmospheric rivers (ARs) (a) and DARK ARs and their children (b) from 60° S to 90° S. From  
 331 left to right: Left panels: AR occurrence (%), Middle and right panels: differences from the Wille vIVT, and the Wille IWV  
 332 and the G&W v4 schemes (percentage points, pp). Hatched white areas south of 85° S mark regions without data in the Wille  
 333 schemes, hatches elsewhere cover non-significant regions (Sect. 2.76). Land-area weighted mean and maximum values are  
 334 indicated below each panel.

### 336 3.2 Direction and orientation of DARK ARs

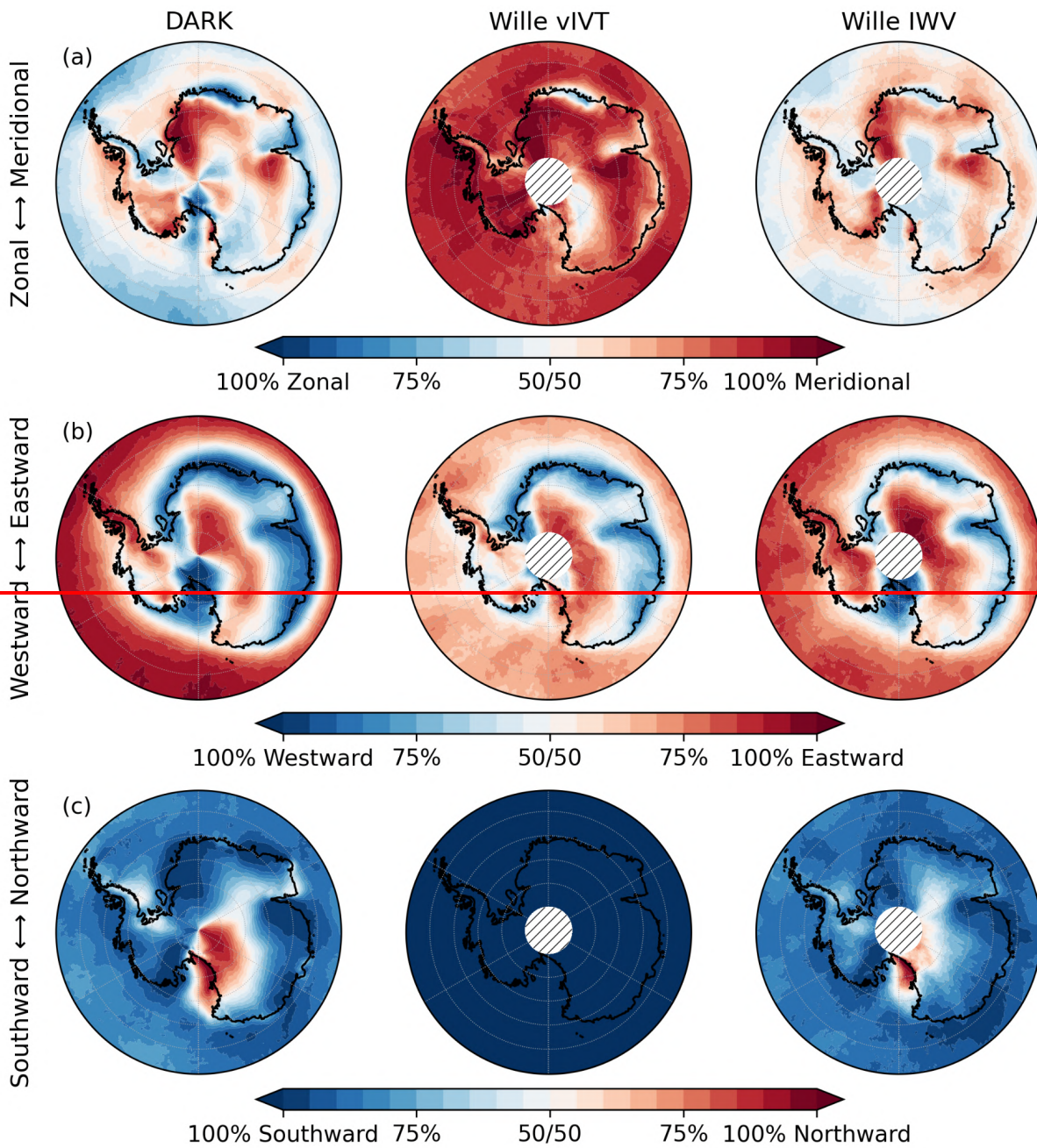
337 DARK ARs exhibit a much wider range of orientations than either Wille schemes while still reproducing well the dominant  
 338 large-scale IVT orientation patterns (zonal versus meridional, and eastward versus westward) captured by Wille IWV (Fig.  
 339 4Fig-3a, c; Sect. 2.5). A majority of Wille vIVT ARs are also detected by DARK, with 64 % agreement over the Southern  
 340 Ocean and about 61 % on average across the AIS (Fig. S5Fig-S3a). The co-detection is strongest where DARK ARs exhibit  
 341 predominantly meridional, southward orientations, such as over southern Dronning Maud Land, Coats Land, and along the  
 342 northern flank of the East Antarctic Ice Divide. However, a substantial fraction of ARs detected by DARK are not captured by

343 Wille vIVT: across the Antarctic Ice Sheet, roughly 67 % of DARK ARs are exclusive to the new detection framework (Fig.  
344 [S5Fig-S3b](#)). These additional detections are particularly frequent from the Ross Ice Shelf to Dome A along the southern flank  
345 of the East Antarctic Ice Divide. In these regions, DARK ARs are mainly northward (Fig. [4Fig-3c](#); and eastward, due to the  
346 influence of the East Antarctic topography and the Coriolis deflection of the pressure-driven circulation) oriented, which is  
347 incompatible with Wille's strict requirement of southward vIVT. Elsewhere across the continent, all three schemes, DARK,  
348 Wille vIVT, and Wille IWV, show predominantly southward-oriented ARs, confirming that most intense moisture transport  
349 toward Antarctica occurs in a poleward direction. Wille vIVT ARs that do occur there generally correspond to relatively strong  
350 meridional, but weak total IVT, since the percentile-based threshold can be met even under low IVT. In contrast, DARK  
351 detects ARs in these sectors because they exceed the 98th-percentile threshold in total IVT, capturing dynamically stronger  
352 but more geometrically complex structures. Compared with Wille IWV, DARK shows a more homogeneous agreement across  
353 the AIS, with up to 90 % co-detection in Dronning Maud Land (Fig. [S5Fig-S3a](#)). This higher overlap reflects the greater  
354 directional flexibility of Wille IWV, which can capture zonal or northward ARs (Fig. [4Fig-3a,c](#)), including those turning over  
355 the Ross and Amery Ice Shelves and along the East Antarctic coastline. However, Wille IWV remains limited by its 20°  
356 meridional-extent criterion, which disfavors fully zonal filaments. Moreover, because IWV represents static moisture rather  
357 than dynamic transport, it detects only about 50 % of DARK ARs in localized regions such as the Dronning Maud Land coast  
358 ([Fig. S5Fig-S3b](#)). These undetected cases typically contain high humidity but insufficient wind to produce large IVT values,  
359 preventing them from meeting the DARK threshold. Overall, Wille vIVT and IWV ARs only partially overlap with DARK  
360 detections. A majority of Wille (vIVT or IWV) ARs are identified by DARK, but many DARK ARs are not detected by Wille  
361 ARDTs. This asymmetry highlights that while the methods share a common physical basis, DARK extends beyond Wille's  
362 directional and geometric constraints, capturing a more dynamically coherent and diverse range of AR geometries, including  
363 curved, zonal, and poleward-turning filaments that were missed by previous frameworks.

364 Compared with G&W v4, DARK shows broadly consistent large-scale IVT orientation patterns across both the Southern  
365 Ocean and the Antarctic continent, although the G&W v4 fields appear noisier over the interior due to the very low number of  
366 detections in these regions.



367



368

369 Figure 43. Fraction of AR time characterized by (a) zonal vs. meridional dominant IVT components ( $|uIVT|$  vs.  $|vIVT|$ ), (b)  
 370 westward vs. eastward  $uIVT$ , and (c) southward vs. northward  $vIVT$  anomalies relative to climatology, for each AR catalogue  
 371 (from left to right: DARK (left), Wille vIVT (middle), and Wille IWV and G&W v4) (right). Hatched white areas south of 85°

372 S mark regions without data in the Wille schemes. Grey shading in the G&W v4 column indicates grid cells where no AR was  
373 detected over the full period.

### 375 3.2 Contribution of ARs to Antarctic precipitation

376  
377 DARK ARs account for an average of 18 % of total AIS precipitation, reaching up to 35 % in some regions (Fig. 5Fig-4a).  
378 Only along the relatively straight, zonally oriented sectors of the East Antarctic coastline, their contribution is comparable to  
379 that of Wille vIVT ARs. In contrast, in areas where the coastline geometry departs from this alignment, particularly within the  
380 major embayments such as the Ross, Ronne–Filchner, and Amery Ice Shelves, DARK ARs contribute to substantially more  
381 precipitation, with enhanced signals extending inland over the catchments located south of the EAID. The only region where  
382 DARK ARs contribute to less precipitation than Wille vIVT ARs is Oates Land.

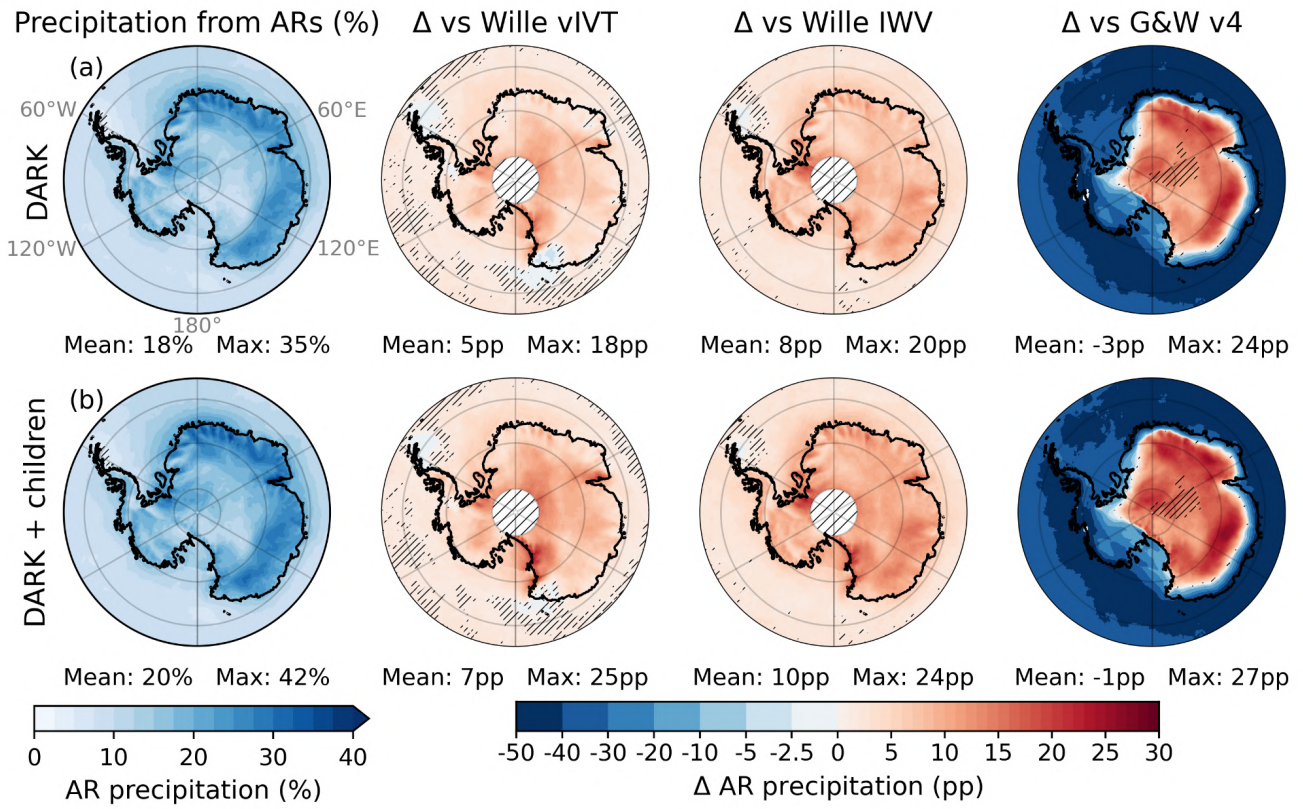
383 On average, DARK ARs deliver 5 (8) pp more precipitation than Wille vIVT (Wille IWV), with local increases up to 18 (20)  
384 pp in the interior, notably near the South Pole and the Transantarctic Mountains. Even when both Wille schemes are combined,  
385 DARK ARs still produce 2 pp more precipitation on average, with local differences reaching up to 15 pp (Fig. S6Fig-S4). The  
386 comparison with G&W v4 reveals spatially contrasting differences that cannot be summarized by the AIS-averaged difference  
387 alone, as the two schemes have fundamentally different detection footprints over Antarctica. Along the coast and over the  
388 WAIS, the very high AR occurrence in G&W v4 translates into substantially more attributed precipitation, locally exceeding  
389 DARK by up to 50 pp. Moving inland, this signal reverses sharply: DARK explains up to 24 pp more precipitation north of  
390 the EAID, where G&W v4 detections drop off rapidly due to its effective hemispheric IVT threshold. This coastal dominance  
391 outweighs the inland gains, yielding a slightly negative AIS-averaged difference of -3 pp (Fig. 5Fig-4a, right column). This  
392 sign reversal reflects the different purposes of the two approaches: G&W v4 was designed for global applicability and captures  
393 intense coastal moisture intrusions, while DARK was specifically designed to monitor AR activity across the full Antarctic  
394 continent, including its interior. Within the DARK framework itself, AR-children contribute little on average (Fig. 5Fig-4b)  
395 but represent a significant additional source within these embayments, most notably over the Amery Ice Shelf and Victoria  
396 Land, where they account for more than 8 % of total AIS precipitation (Fig. S2b).

397 In this analysis, precipitation occurring on the day of AR landfall ( $D_0$ ) and the following day ( $D_{+1}$ ) is attributed to ARs  
398 throughout this study (Sect. 2.4), and to ARs and their children when using the DARK+children framework, consistent with  
399 common practice (Wille et al., 2021; Maclennan et al., 2022). When AR-children are included, however, a comparable AIS-  
400 averaged share of precipitation is obtained (Fig. S7Fig-S5) even when considering precipitation associated with DARK ARs  
401 and their children on the day of landfall alone ( $D_0$ ), compared to attributing precipitation to DARK ARs without including AR-  
402 children over both the day of landfall ( $D_0$ ) and the following day ( $D_{+1}$ ). This reflects not a temporal substitution, but a spatial  
403 refinement: AR-children explicitly capture the inland propagation and dissipation of moisture that, in previous approaches,

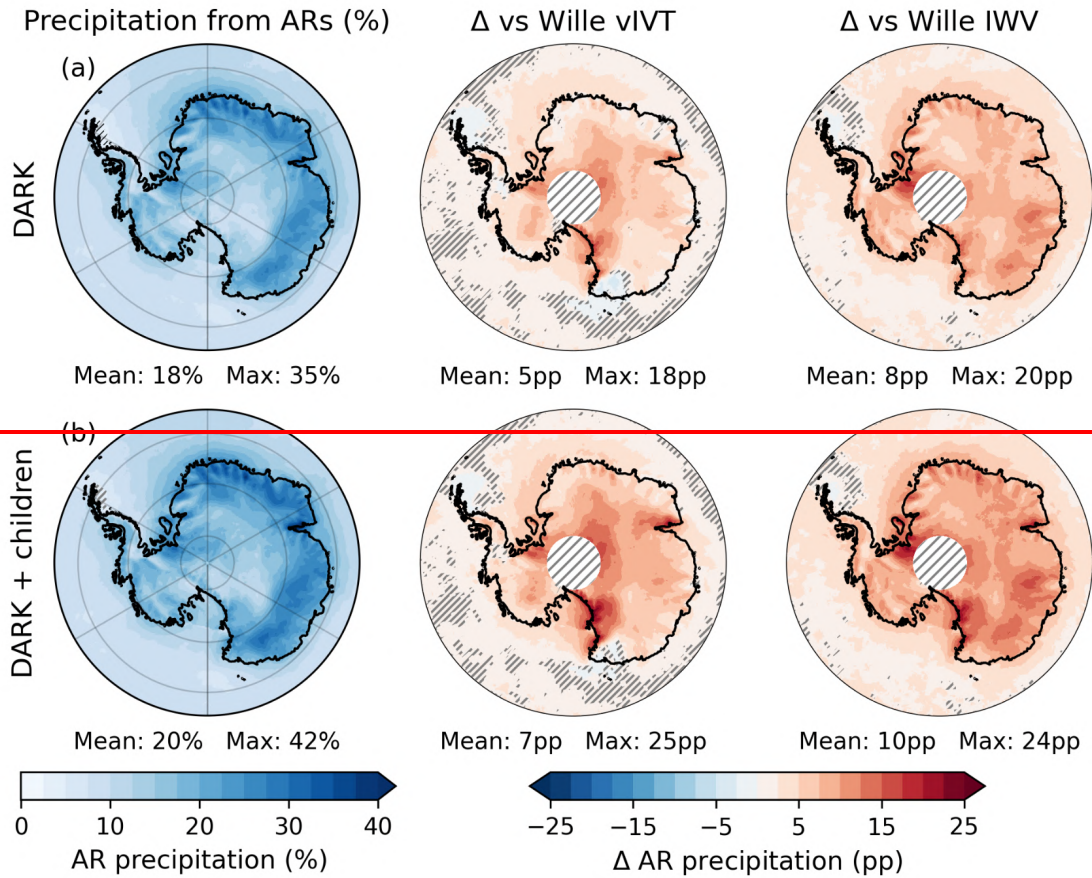
404 was only approximated by extending the temporal attribution window beyond landfall. Their inclusion therefore provides a  
405 more physically consistent representation of post-landfall hydrological impacts.

406

407



408

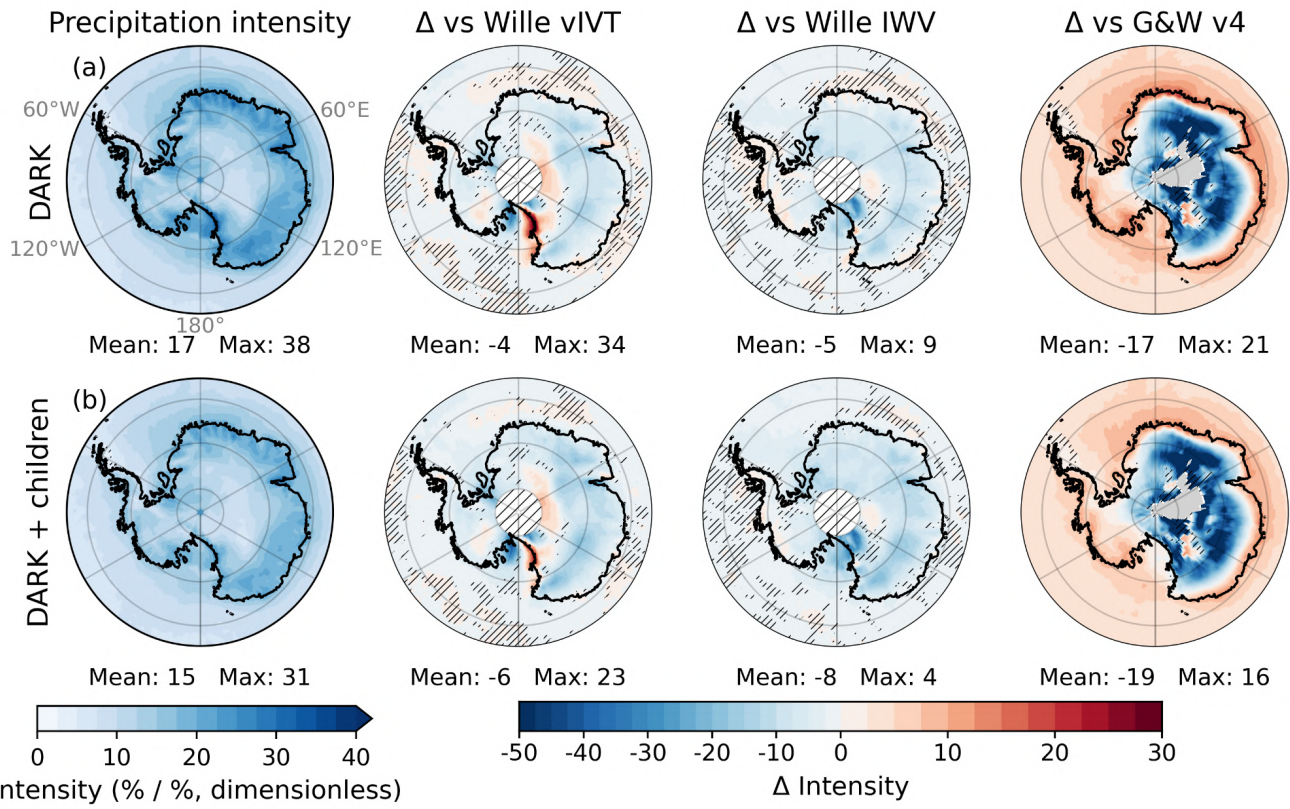


409  
 410 Figure 54. Share of total precipitation attributed (Sect. 2.4) to (a) DARK ARs and (b) DARK ARs and their children. From  
 411 left to right Left panels: percentage of precipitation from ARs, Middle and right panels: differences from the Wille vIVT, and  
 412 the Wille IWV, and the G&W v4 schemes (pp). Antarctic land-only (inside-coastline) mean and maximum values are reported  
 413 below each panel. Hatched white areas south of 85° S mark regions without data in the Wille schemes, hatches elsewhere  
 414 cover non-significant regions (Sect. 2.76).

415  
 416 While DARK ARs contribute more to precipitation than either Wille scheme across most of the AIS, this increase primarily  
 417 reflects their higher occurrence frequency rather than higher precipitation per event (Fig. 6Fig. 5a). When normalized by AR  
 418 occurrence, that is, expressed as the ratio of AR-related precipitation (%) to AR occurrence (%), the mean precipitation  
 419 intensity (pp pp<sup>-1</sup>, dimensionless) associated with DARK ARs is slightly lower overall than in both Wille schemes (around -  
 420 5). Relative to Wille IWV, precipitation intensity is lower across the AIS in a broadly uniform pattern. However, relative to  
 421 Wille vIVT, differences are more heterogeneous: intensity is reduced over most of the AIS but locally enhanced over the  
 422 Amery Ice Shelf and south of the EAID, peaking along the Ross sector of the Transantarctic Mountains (up to 34). When

423 DARK ARs and their associated children are considered together, the overall AR intensity further decreases, although they  
424 remain more intense than Wille ARs in the latter regions (~~Fig. 6~~~~Fig. 5~~b).

425  
426 The comparison with G&W v4 mirrors the spatial heterogeneity seen in total precipitation. Along the coast and over the WAIS,  
427 DARK ARs are more intense than G&W v4 ARs (positive differences), consistent with DARK having fewer but still highly  
428 impactful detections in these regions. Inland, the picture reverses: intensity differences become negative over large parts of the  
429 East Antarctic interior, reaching below -50 in some areas. These strongly negative values, however, must be interpreted with  
430 caution, as they correspond to regions where G&W v4 detects very few AR days over the full period (fewer than 35 where  
431 differences exceed -50, fewer than 100 where they exceed -30; Fig. S4). In these areas, the small sample of G&W v4  
432 detections consists almost exclusively of the most intense inland moisture intrusions, inflating their mean intensity relative to  
433 DARK. Overall, this confirms that G&W v4 selectively captures the most intense moisture intrusions at the coast and in the  
434 rare inland locations where IVT remains sufficiently high, while missing the broader population of intrusions that DARK and  
435 the Wille schemes track from the coast into the interior.



436

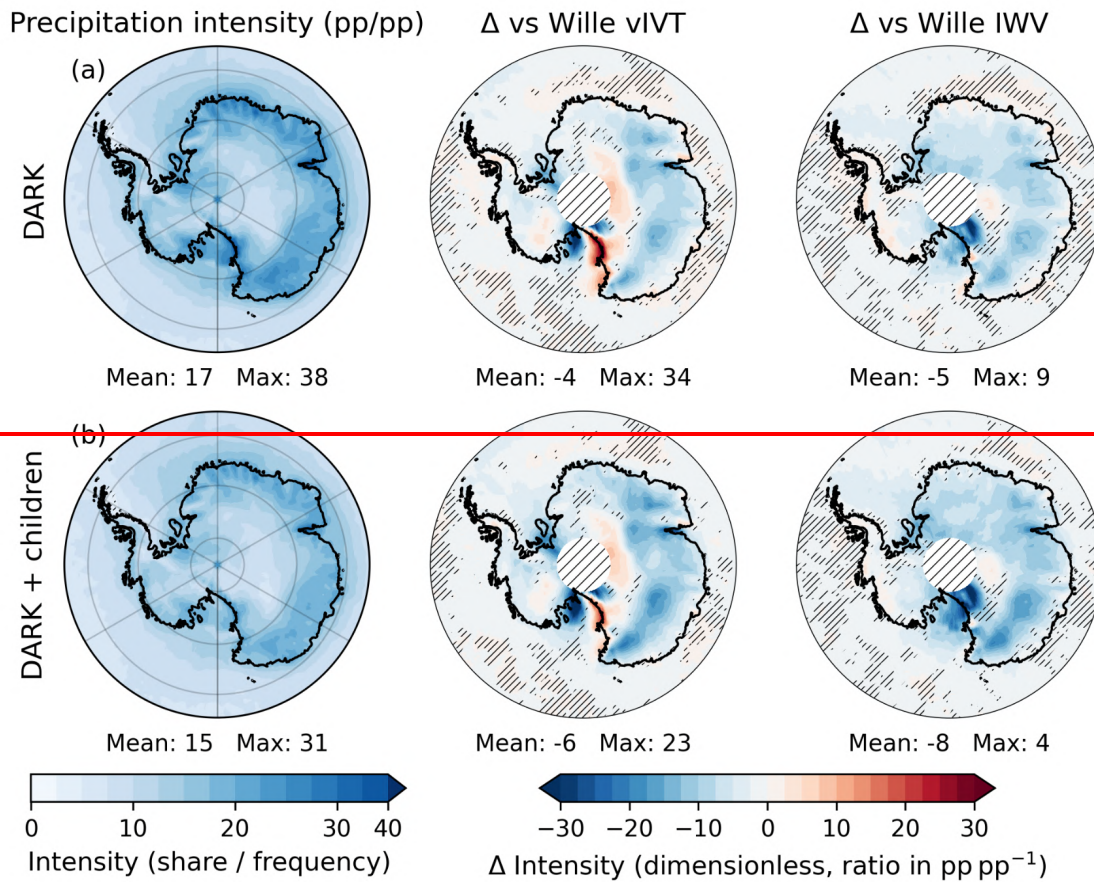


Figure 65. Normalized AR precipitation intensity, defined as the ratio between the percentage of precipitation from ARs (Fig. 3Fig-2) and AR frequency (Fig. 3Fig-2, unitless), for (a) DARK ARs and (b) DARK ARs and their children. From left to right: Middle and right panels: differences from the Wille vIVT, and the Wille IWV, and the G&W v4 schemes (pp). Antarctic land-only mean and maximum values are reported below each panel. Hatched white areas south of 85° S mark regions without data in the Wille schemes, hatches elsewhere cover non-significant regions (Sect. 2.7).

### 3.3 Contribution to extreme events

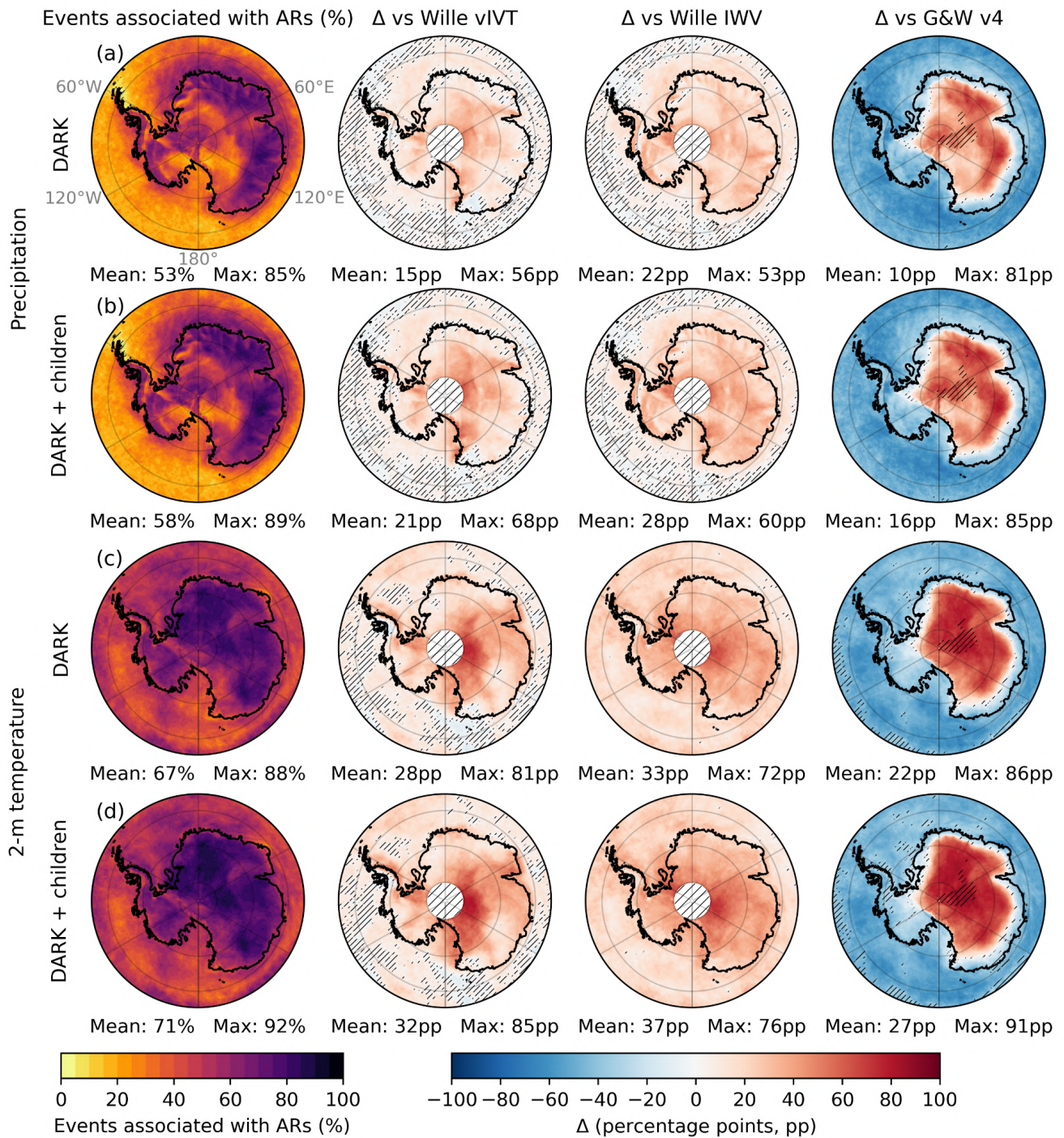
DARK ARs are associated with 53 % of extreme (Sect. 2.4) precipitation days on average (Fig. 7Fig-6a), with local values reaching up to 85 % inland of the East Antarctic coast and decreasing toward Dome C. Although the mean precipitation per AR event is lower (Sect. 3.2), the DARK scheme captures a substantially larger proportion of the most intense precipitation anomalies than either Wille scheme. Compared to Wille vIVT, the association fraction is higher by 15 pp on average and locally by up to 56 pp south of the EAID, with only a few small areas showing slightly weaker associations, the largest being Oates Land. Relative to Wille IWV, the increase is more spatially homogeneous, with the largest differences following

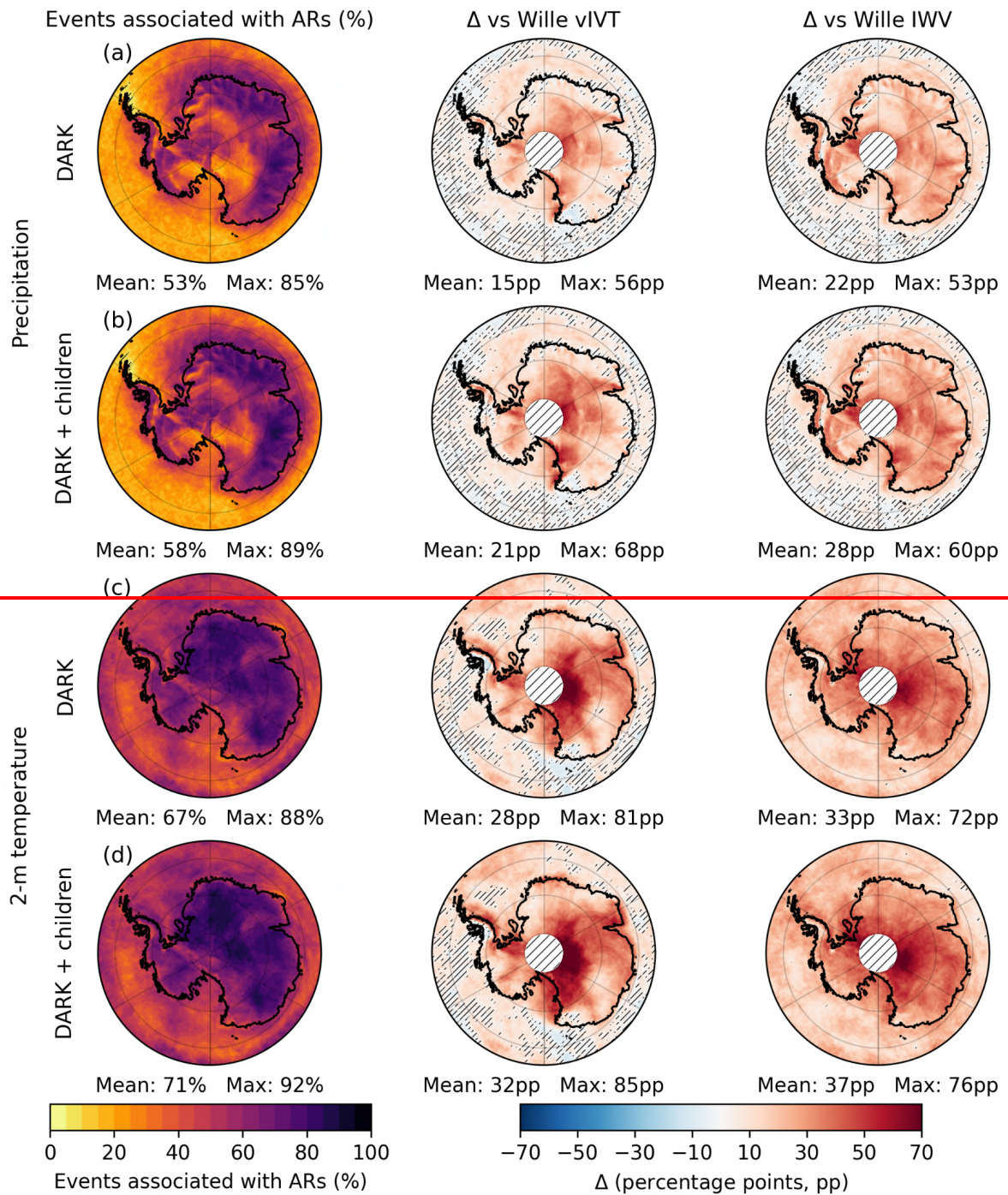
450 topography, particularly over Queen Elizabeth Land. This pattern indicates that DARK, like Wille vIVT, better represents  
451 topographically induced precipitation linked to moisture transport rather than static humidity. Compared with G&W v4, DARK  
452 explains on average 10 pp more extreme precipitation days across the AIS, with gains up to 81 pp inland. Along the coast and  
453 over the WAIS, G&W v4 associates more extreme days with ARs, consistent with its very high detection frequency in these  
454 regions. However, unlike for total precipitation, the AIS-averaged difference remains positive, reflecting the fact that many of  
455 the numerous G&W v4 coastal detections are associated with non-extreme precipitation events that do not reach the top 1%  
456 threshold. Including AR-children increases the mean association by only about 5 pp (Fig. 7Fig-6a,b), but they remain locally  
457 significant, forming broad hotspots over the Amery Ice Shelf and across Victoria Land, where they account for more than 15  
458 %, and locally up to 20 %, of extreme precipitation days (Fig. S8Fig-S6). These regions represent the strongest and most  
459 spatially extensive contributions of AR-children, while more localized contributions also occur south of the EAID, where post-  
460 landfall moisture remnants sustain intense precipitation after the parent AR dissipates.

461 DARK ARs are associated with 67 % of extreme daily maximum temperature events on average (Sect. 2.4; Fig. 7Fig-6c),  
462 with local values exceeding 80 % near Dome C and over Dronning Maud Land. Compared to the Wille schemes, DARK  
463 increases the association fraction by more than 28 pp on average. The gain is spatially uniform relative to Wille IWV and more  
464 spatially contrasted compared to Wille vIVT, with the largest improvements south of the EAID. Compared with G&W v4,  
465 DARK explains on average 22 pp more extreme temperature days, with a spatially uniform inland advantage reflecting  
466 DARK's more consistent continental coverage. As with precipitation extremes, G&W v4 explains more along the coast, but  
467 the AIS-averaged difference remains strongly positive, consistent with DARK's broader and more homogeneous detection  
468 across the interior. Including AR-children further raises the mean association to approximately 71 % (Fig. 7Fig-6d), primarily  
469 through a uniform increase of about 4 pp across most of the AIS. In several regions, this leads to association fractions exceeding  
470 90 % locally, while the largest increases occur over Victoria Land and the Ross Ice Shelf–McMurdo area, where AR-children  
471 contribute up to 20 pp of additional extreme temperature events. This reflects the persistence of warm, moist air masses  
472 following AR landfall (Fig. S8Fig-S6).

473 Compound (precipitation and 2 m air temperature) extremes (Sect. 2.4) occur widely across Antarctica but are absent leeward  
474 of the Antarctic Peninsula, where strong foehn winds produce warm but dry conditions (Fig. S9Fig-S7). DARK ARs are  
475 associated with approximately 78 % of compound extremes on average (Fig. 8Fig-7a) and with nearly 100 % across broad  
476 sectors of East Antarctica. DARK identifies substantially more inland events than Wille vIVT, which captures many compound  
477 events along the coast but misses large interior regions south of the EAID, from southern Dronning Maud Land to Victoria  
478 Land and around the Amery Ice Shelf. Compared with G&W v4, DARK explains on average 30 pp more compound extremes  
479 across the AIS, with the same coastal-to-inland polarity as for precipitation and temperature extremes. Including AR-children  
480 increases the mean association modestly (by about 3 pp) but introduces a distinct new hotspot over Victoria Land (Fig. 8Fig-  
481 7b), where AR-children contribute to more than 20 pp of additional compound extremes (Fig. S8Fig-S6). Notably, Victoria

482 Land is also one of the two main regions of frequent compound events across the continent, although such events remain rare  
483 overall (fewer than 0.5 % of days: [Fig. S9](#)~~Fig. S7~~).





485

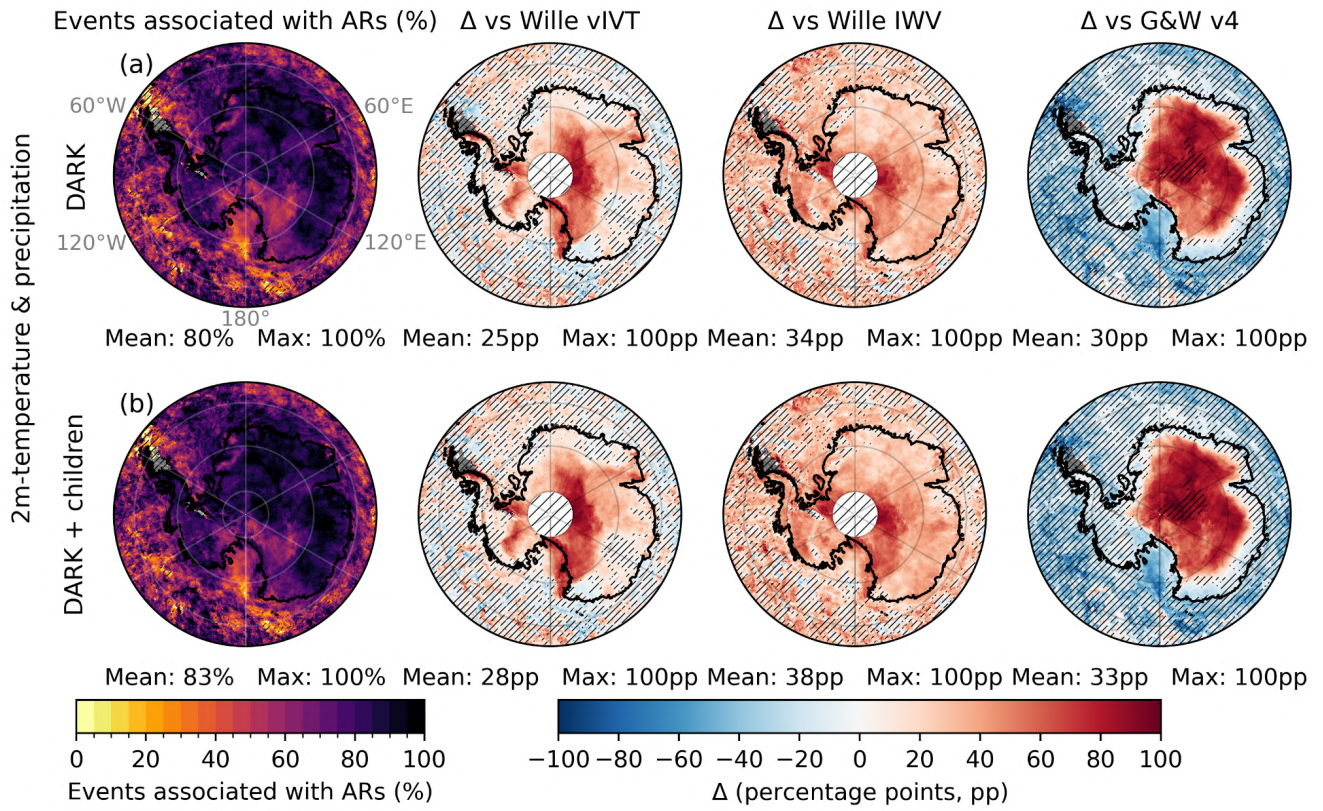
486

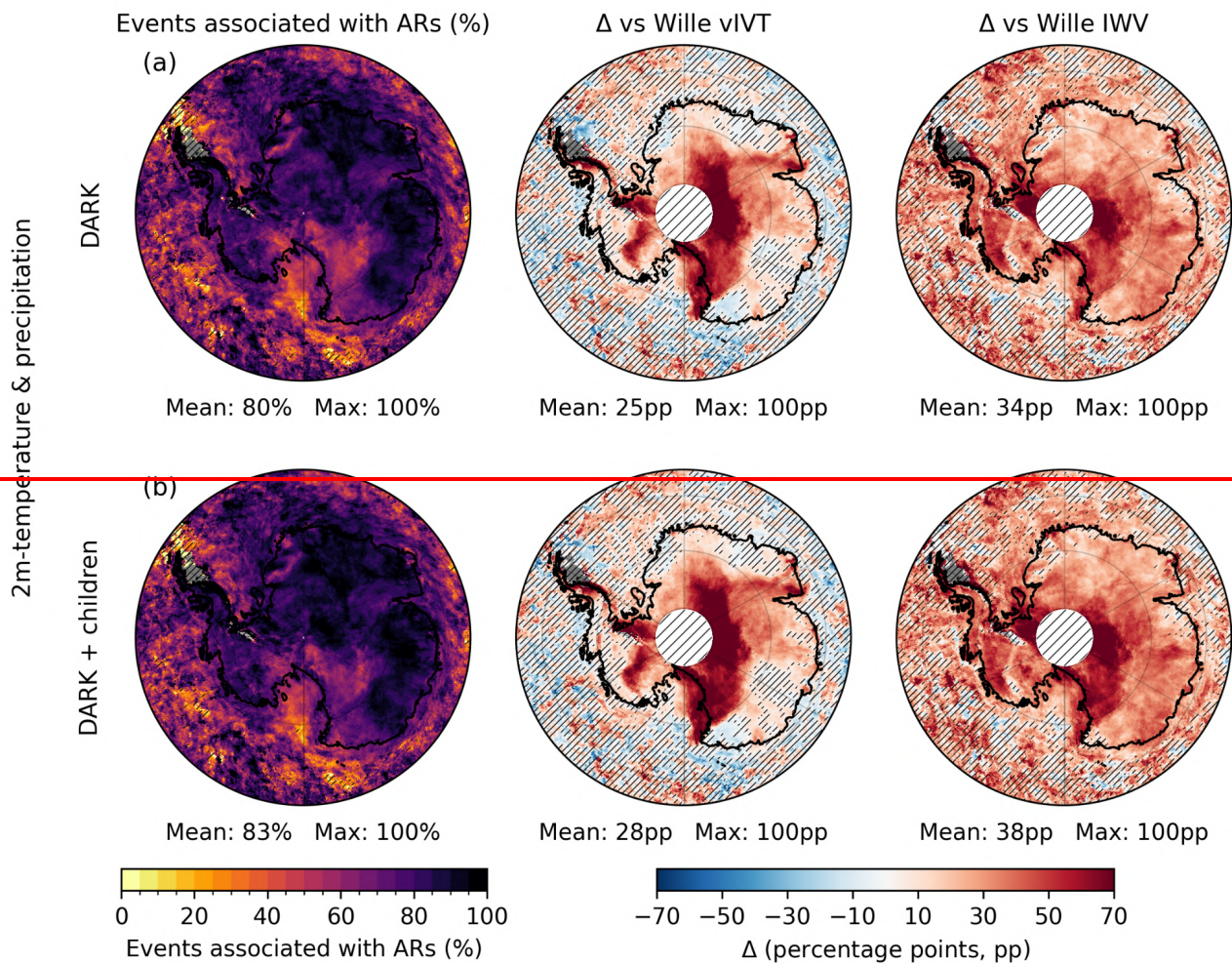
487

488

Figure 76. Fraction of 99th-percentile anomaly days associated with DARK ARs for precipitation (rows a–b) and 2 m temperature (rows c–d). Within each variable, the first row shows DARK ARs and the second row shows DARK ARs + children. Columns show (left to right) the absolute fraction of extremes and the differences relative to the Wille vIVT, ~~and the~~

489 Wille IWV, [and the G&W v4](#) schemes (percentage points, pp). Antarctic land-only mean and maximum values are reported  
490 below each panel. Hatched white areas south of 85° S mark regions without data in the Wille schemes; hatched overlays  
491 indicate non-significant values ([Sect. 2.7](#)); grey shading indicates grid cells with no detected extremes.  
492





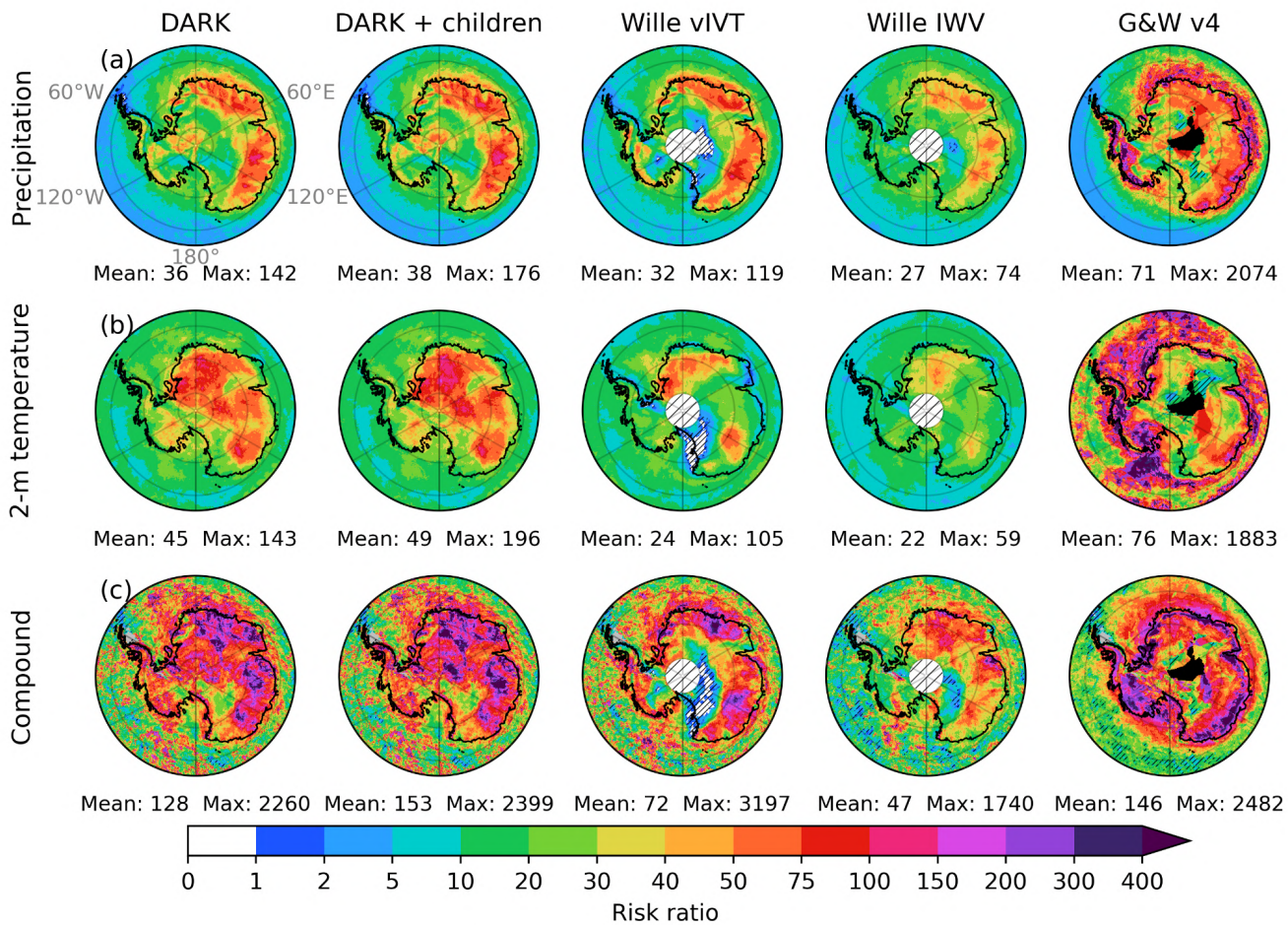
494 Figure 87. Fraction of compound extreme days combining 99th-percentile precipitation and 2 m air temperature anomalies  
 495 associated with DARK ARs. Row (a) shows DARK ARs and row (b) shows DARK ARs and their+ children. FColumns  
 496 display (from left to right:) the absolute fraction of compound extremes and the differences relative to the Wille vIVT, and the  
 497 Wille IWV, and the G&W v4 schemes (percentage points, pp). Antarctic land-only mean and maximum values are reported  
 498 below each panel. Hatched white areas south of 85° S mark regions without data in the Wille schemes; hatched overlays  
 499 indicate non-significant values (Sect. 2.7); grey shading indicates grid cells with no detected compound extremes.

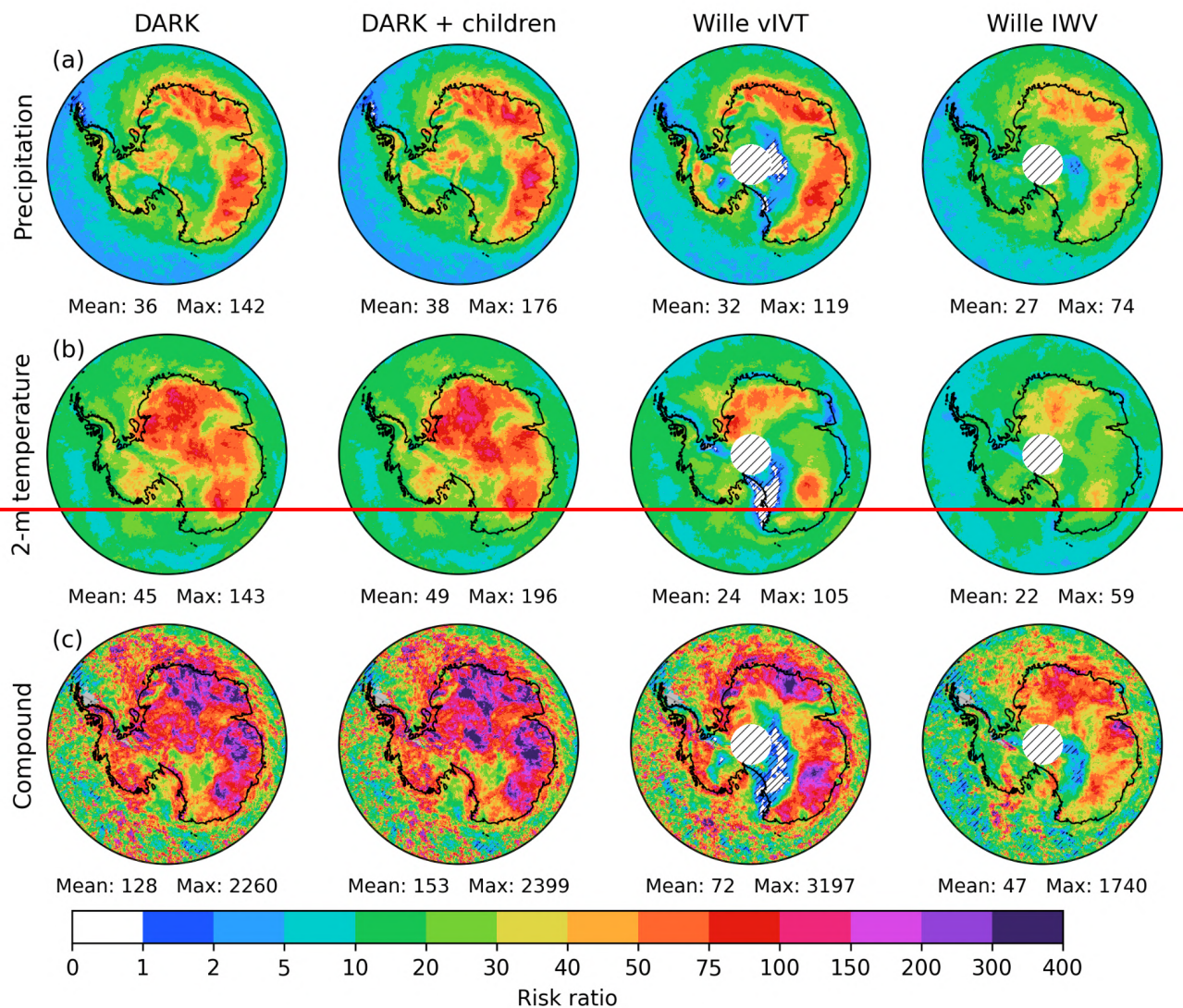
501 Risk ratios (RR) are next used to account for differences in AR occurrence frequency (Sect. 2.65). For precipitation, DARK  
 502 yields RR values comparable to or higher than those of the Wille schemes across most of the AIS (Fig. 9Fig-8a), indicating  
 503 that extreme precipitation is about 30 times more likely during an AR, independently from the selected ARDT. The spatial  
 504 pattern closely resembles that of Wille vIVT, with the highest values north of the EAID and local peaks reaching 142. However,  
 505 for 2 m air temperature (Fig. 9Fig-8b), the similarity with Wille's ARDTs is weaker. While DARK reproduces the main

506 hotspots seen in Wille's ARDTs, RRs are considerably larger over a much wider area. The Antarctic-wide mean RR reaches  
507 45 (roughly twice the Wille means), with local maxima up to 143, demonstrating that DARK not only amplifies the temperature  
508 hotspots detected by Wille vIVT and IWV but also identifies additional regions of strong AR influence beyond those captured  
509 by the original scheme. For compound extremes (Fig. 9Fig-8c), DARK produces a markedly higher RR than Wille's ARDTs,  
510 with an Antarctic-wide mean of 128, almost double that of Wille's 's ARDTs, and local maxima exceeding  $10^3$ , highlighting  
511 the dominant influence of ARs on concurrent warm and wet extremes. Including AR-children further increases both mean and  
512 peak RR for precipitation, temperature, and compound events, illustrating that post-landfall moisture remnants can cause  
513 extremes after the parent AR loses coherence.

514 The G&W v4 ARDT yields substantially larger RR values across the AIS for all variables (Fig. 9). For precipitation (Fig. 9a),  
515 the Antarctic-wide mean RR reaches 71, more than twice the values obtained with DARK and the Wille schemes. A similar  
516 difference is found for 2 m air temperature (Fig. 9b), where the mean RR rises to 76. For compound extremes (Fig. 9c), the  
517 Antarctic-wide mean RR reaches 146. These large ratios reflect a very strong statistical association between G&W v4 ARs  
518 and extreme events. However, their magnitude is strongly shaped by the particular spatial structure of G&W v4 detection  
519 frequency over Antarctica, with far more AR days than DARK or the Wille schemes at the coast and far fewer inland, which  
520 creates strongly contrasted AR and non-AR pools that mechanically amplify RR in both regimes. The spatial coincidence  
521 between the largest RR values and the regions of highest G&W v4 detection frequency is a direct consequence of these  
522 contrasts, rather than evidence of a stronger physical association. Consequently, the RR values from G&W v4 are less directly  
523 comparable to those obtained with DARK and Wille's ARDTs.

524





526

527

528

529

530

531

532

533

Figure 98. Risk ratio (RR; see Sect. 2.65) of 99th-percentile anomalies during AR conditions for (a) 2 m air temperature, (b) precipitation, and (c) compound events (precipitation + temperature; see Sect. 2.4). Columns correspond to DARK ARs, DARK ARs and their children, Wille vIVT, ~~and~~ Wille IWV, and G&W v4 ARs. Values of RR > 1 indicate an increased likelihood of extremes under AR conditions. Grey areas indicate grid cells without detected compound extremes, hatches indicate non-significant RR (Sect. 2.76), black shading in the G&W v4 column indicates grid cells where no AR was detected over the full period.

### 3.4 Regional case studies

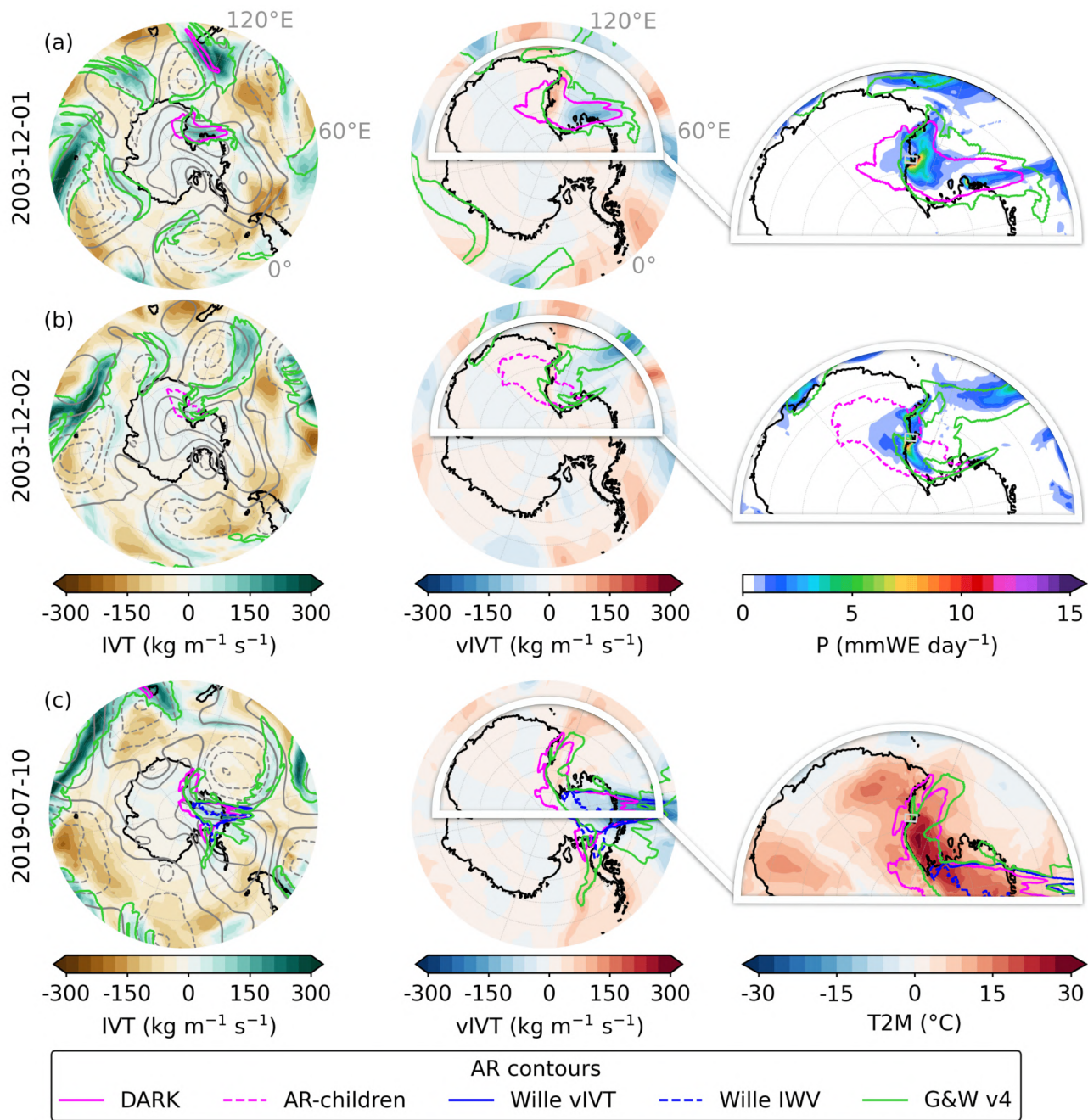
To illustrate the performance of the DARK framework during intense to extreme weather events, we analyze representative cases. The first case study focuses on the McMurdo region, a well-known area situated between the Ross Ice Shelf and Victoria Land, both of which show strong enhancement in DARK relative to Wille’s ARDTs. The second case study examines ARs detected south of the EAID, including those crossing the South Pole.

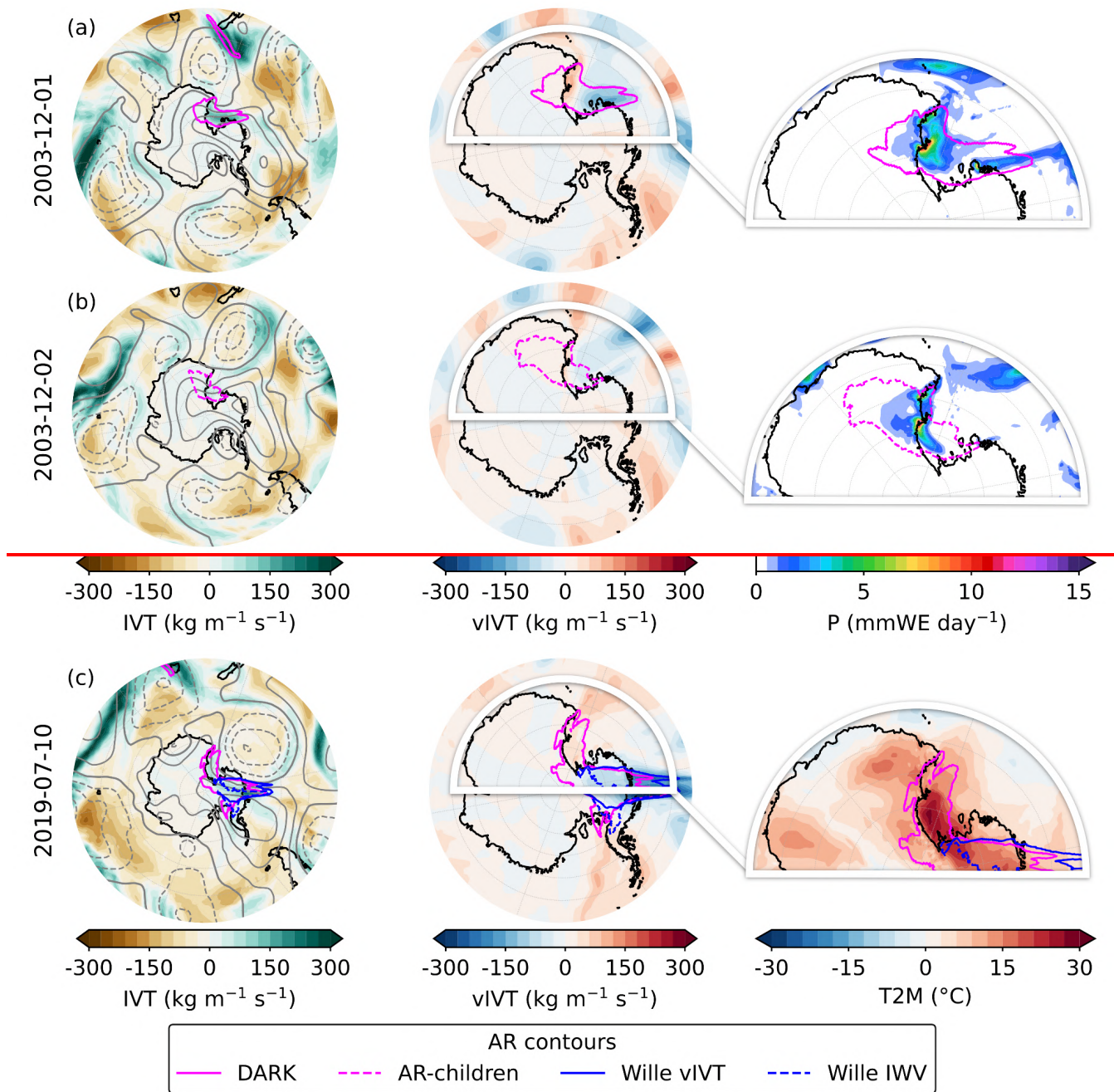
#### 3.4.1 Extreme events in the McMurdo–Dry Valleys region

The first case study focuses on the McMurdo–Dry Valleys domain (160–168° E, 78.5–77.5° S), where two exceptional events exemplify the synoptic conditions driving major precipitation and temperature extremes.

On 1 December 2003 (Fig. 10Fig. 9a), the McMurdo–Dry Valleys region recorded more than 16 mm of precipitation, exceptionally high for this arid environment, representing the largest daily precipitation total in the 1979–2024 ERA5 dataset. Including the following day (2 December 2003, with more than 12 mm, corresponding to the 99.9th percentile), the two day total accounts for over 14 % of the annual precipitation in 2003. The 500-hPa geopotential height anomalies reveal a broad anticyclonic circulation spanning the Antarctic interior from the Bellingshausen Sea to Dome C, with a maximum over Marie Byrd Land. ~~The western flank of this ridge~~~~A deep trough northwest of the Ross Sea and another farther north~~ directed a zonal moisture flux ~~from the South Pacific~~ into the western Ross Sea sector. Upon encountering the Transantarctic Mountains, this flux curved equatorward and westward, producing intense coastal precipitation. The DARK scheme captures the full curvature of this moisture filament as it arcs inland over Victoria Land, while neither Wille vIVT nor Wille IWV detect the equatorward-turning portion (Fig. 10Fig. 9a). ~~G&W v4 detects a broader moisture feature over the Ross Sea and Victoria Land, capturing part of the zonal flux but not the full inland portion of what DARK classifies as an AR. Notably, G&W v4 flags numerous AR objects across the Southern Hemisphere on this date, considerably more than DARK or the Wille schemes, reflecting its lower effective IVT threshold in high-IVT coastal regions.~~ The precipitation maximum coincides with the AR’s interaction with the Transantarctic Mountains, followed by a sharp inland decline in IVT consistent with strong orographic precipitation. By 2 December, ~~a deep trough northwest of the Ross Sea had aligned and channeled moisture from the South Pacific toward the Ross Ice Shelf, sustaining the precipitation event.~~ The main AR filament had dissipated, leaving behind a remnant classified as an AR-child, ~~while G&W v4 captures this day as a full AR extending from the South Pacific, detecting the entire moisture import corridor where DARK identifies only the inland tip.~~ Despite its smaller spatial extent, this remnant produced more than 12 mm of precipitation, still within the top 0.1 % of daily values. This demonstrates that post-landfall AR fragments can sustain extreme precipitation even after the parent AR loses coherence. This event highlights the importance of explicitly identifying and tracking AR-children, which can prolong the hydrological impacts of ARs well beyond their formal duration.

565 On 9 July 2019 (Fig. 10Fig-9b), an exceptional temperature extreme affected the Ross Ice Shelf region, including the McMurdo  
566 area, with 2 m air temperature daily anomalies peaking at +27.9 °C in the McMurdo-Dry Valleys. This event represents the  
567 largest daily-mean temperature anomaly in the 1979–2024 ERA5 record, and exceeded +31 °C over parts of the shelf. The  
568 500-hPa geopotential height anomalies show an extensive anticyclonic structure extending from the southern tip of South  
569 America across the Antarctic continent and into the southern Indian Ocean, centered over the Antarctic interior. A deep trough  
570 north of the Ross Sea directed moist air from the South Pacific toward the Ross Ice Shelf, where the flow was deflected by the  
571 topography of the eastern Ross sector. As the IVT cyclonically curved along the Transantarctic Mountains, leading to  
572 equatorward fluxes off the coasts of Victoria Land, the strongest temperature anomalies occurred and peaked over the Ross  
573 Ice Shelf. DARK ARs capture the complete curved moisture transport pathway responsible for this event, whereas the Wille  
574 schemes detect only the initial southward intrusion and miss the equatorward-turning segment beneath which the peak  
575 temperature anomalies occurred. G&W v4 detects the initial southward intrusion from the mid-latitudes and, like DARK,  
576 captures the moisture transport toward the Ross Ice Shelf where the peak temperature anomalies occurred, but its detection  
577 stops at the coastline. As on 1 December 2003, G&W v4 flags numerous AR objects across the hemisphere on this date, in  
578 contrast to the more sparse detections of DARK and the Wille schemes.





580

581 Figure 109. Daily composites of the most intense (a–b) precipitation and (c) temperature events in the McMurdo–Dry Valleys  
 582 region (160–168° E, 78.5–77.5° S, [grey window in the third column panels](#)). Panels (a) and (b) correspond to 1 and 2 December  
 583 2003, respectively, showing the evolution of the same precipitation event, while panel (c) shows the temperature event on 9  
 584 July 2019. Each column displays, from left to right: integrated vapor transport (IVT) anomaly ( $\text{kg m}^{-1} \text{s}^{-1}$ ), meridional IVT

(vIVT) anomaly ( $\text{kg m}^{-1} \text{s}^{-1}$ ), and (a–b) daily precipitation ( $\text{mm w.e. day}^{-1}$ ) or (c) 2 m air temperature anomaly ( $^{\circ}\text{C}$ ). Grey contours in the first column indicate 500-hPa geopotential-height anomalies (m; solid = positive, dashed = negative) at 100-m intervals. DARK ARs (solid magenta) and their children (dashed magenta) are shown together with Wille ARs (solid blue = vIVT; dashed blue = IWV) and G&W v4 ARs (limegreen). For each day, AR contours represent the maximum spatial extent of each AR type across all 6-hourly time steps (i.e., the union of all detected positions within the day). White-shaded contours in the middle panels outline the domain shown in the rightmost panels.

### 3.4.2 ARs reaching the South Pole

One of the major advancements of the DARK framework is its ability to detect ARs reaching the South Pole, whereas previous schemes such as Wille vIVT and IWV ceased detection at  $85^{\circ}$  S. In ERA5, IVT vectors become ill-defined exactly at  $90^{\circ}$  S because of the coordinate singularity, which causes an artificial drop in detections at the pole. Nevertheless, DARK captures continuous poleward moisture transport all the way to the South Pole, enabling for the first time a physically consistent identification of ARs in this region. To illustrate this, we examine three events detected by DARK near the pole.

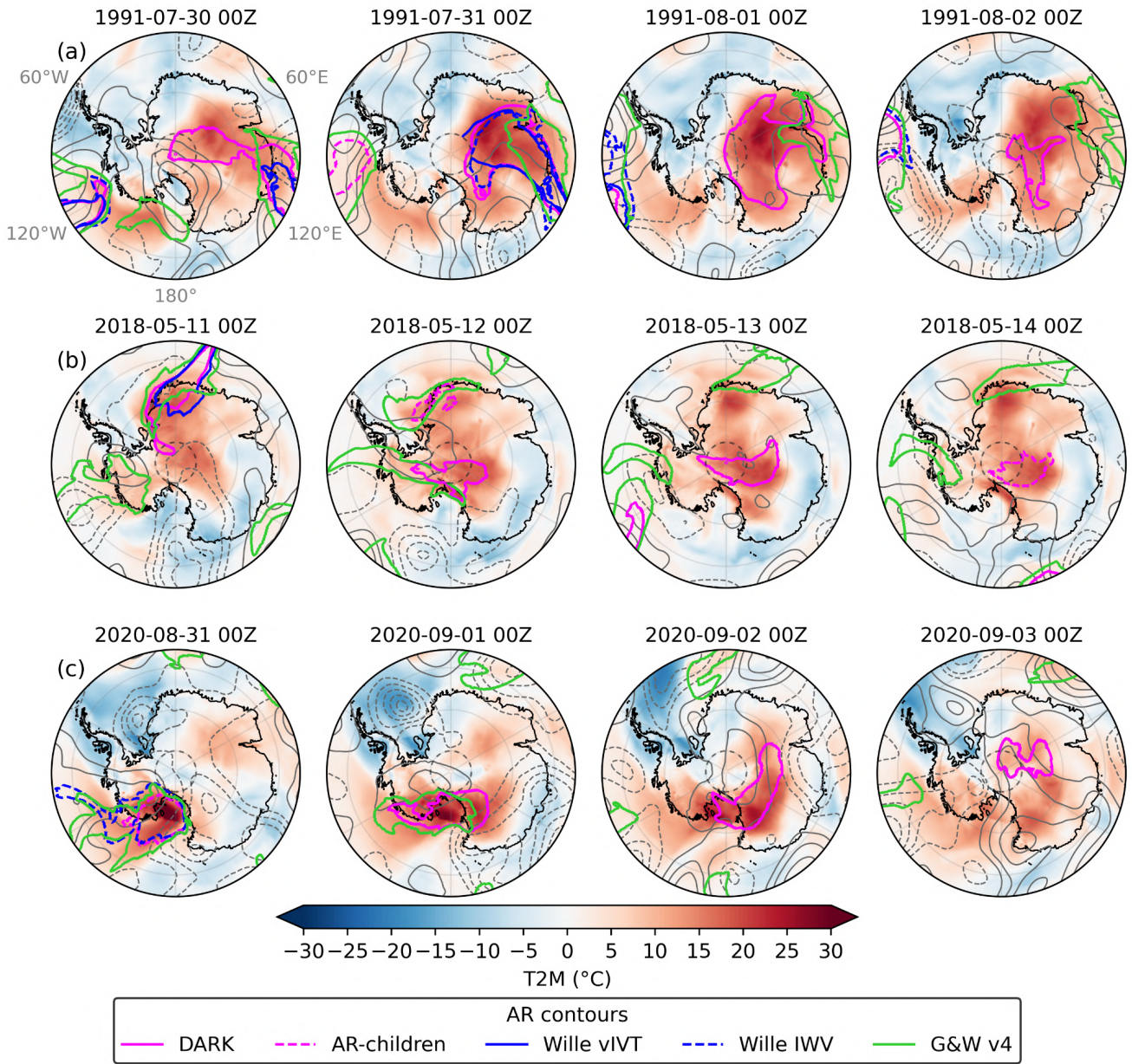
On 30 July 1991 (Fig. 110a), a DARK AR was detected extending from the Princess Elizabeth Land coast across the Antarctic interior to the South Pole. The synoptic configuration featured two centers of action, with a low-pressure system east of Princess Elizabeth Land and a high-pressure system farther east, jointly channeling the moisture plume poleward in a roller-like pattern. Both Wille vIVT and DARK identified ARs along this corridor on that day. However, the Wille vIVT AR stopped at the coast as the meridional IVT component weakened below the 98th percentile and the flow turned more zonal toward Dome A and the South Pole. Yet, the total IVT remained strong, allowing DARK to maintain continuous detection inland. G&W v4 detects multiple ARs around the continent on this date, including the AR of interest, but its detection stops shortly after the coastline. Under the AR footprint, 2 m air temperature anomalies already reached around  $+20^{\circ}\text{C}$ , reflecting the strong advection of warm, moist air from lower latitudes. On the following day, the IVT flow advanced farther across the East Antarctic Plateau. Both Wille and DARK detected ARs from the Princess Elizabeth Land coast over Dome A, with their extent broadening to cover areas from Dronning Maud Land to Victoria Land, reaching latitudes as far south as  $85^{\circ}$  S. G&W v4 follows the moisture plume slightly further inland than on the previous day. Temperature anomalies intensified in step with the AR progression, spreading across the southern flank of the EAID. By the third day, the Wille ARs were no longer detected, while the DARK AR spanned a broad region south of the EAID, reaching the South Pole with a tail still visible along the East Antarctic coast. G&W v4 had already regressed to the coastline, failing to track the moisture transport over the interior where the strongest temperature anomalies, approaching  $+27^{\circ}\text{C}$ , were now concentrated beneath and slightly downstream of the DARK AR core. only the DARK AR remained, spanning a broad region south of the EAID and extending to the South Pole, with a tail still visible along the East Antarctic coast. The strongest temperature anomalies, approaching  $+27^{\circ}\text{C}$ , were recorded at this stage beneath and slightly downstream of the AR core. By the fourth day, the feature had contracted into a thinner

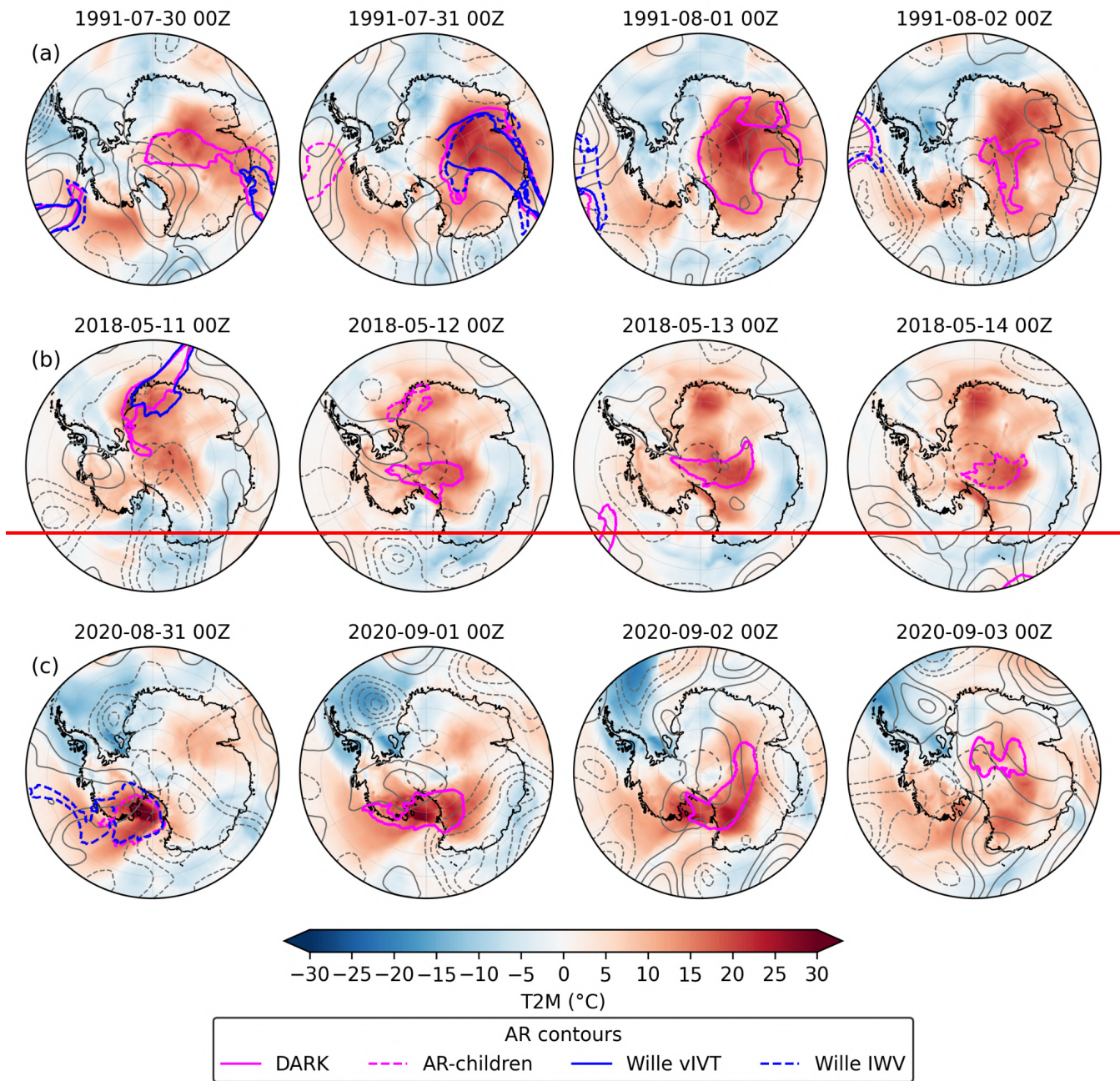
618 filament along the southern flank of the EAID, while the residual warm anomalies persisted in the area previously impacted  
619 by the main AR.

620 On 11 May 2018 (Fig. 11**9**b), intense moisture transport was directed toward Dronning Maud Land, similarly driven by a  
621 marked pressure dipole, with a high-pressure system to the east and a low to the west. Both Wille vIVT and DARK detect ARs  
622 in this configuration, but the DARK AR extends farther inland, reaching Queen Elizabeth Land and up to 87° S. G&W v4  
623 follows the moisture transport more closely than the Wille schemes, detecting the AR along the Queen Elizabeth Land coastline  
624 and the Ronne-Filchner Ice Shelf. It also captures an additional AR approaching from the WAIS that is not detected by DARK  
625 or the Wille schemes, which may represent the precursor moisture flux that evolves into the DARK AR over the South Pole  
626 on the following day. This event coincides with widespread positive 2 m air temperature anomalies across most of the Antarctic  
627 Ice Sheet, except along the East Antarctic coast from Victoria Land to the Amery Ice Shelf. On the following day, no Wille  
628 AR was detected, while the DARK AR had evolved and split into two structures: an AR over the South Pole, just north of the  
629 Ross Ice Shelf where surface temperatures continued to rise, and an AR-child~~ren~~ along the original AR path over Dronning  
630 Maud Land. G&W v4 no longer detects the interior feature, consistent with its inland detection limitations. By the third day,  
631 only the main DARK AR remained, now centered over and slightly beyond the South Pole, having crossed the EAID before  
632 being deflected westward by the topography. Beneath this AR, 2 m air temperature anomalies intensified further, locally  
633 reaching +20 °C. By the fourth day, the AR had decayed into a smaller AR-child, yet the warm anomalies remained strong,  
634 particularly within these moisture remnants. Notably, after the AR had moved away from Dronning Maud Land, temperature  
635 anomalies there continued to increase through days 3 and 4, suggesting that the warm air mass and its heat content persisted  
636 well after the main AR passage.

637 On 31 August 2020 (Fig. 11**9**c), a moisture-laden plume reached the Ross Ice Shelf, similarly guided by a high-pressure system  
638 centered over West Antarctica and a low-pressure system over Victoria Land. The ~~disorganized non-circular~~  
639 systems, with wavy rather than well-defined closed centers of action, reflects relatively weak wind speeds, which likely  
640 explains why this event is not detected by either vIVT or DARK. The event was detected as a Wille IWV AR and as a G&W  
641 v4 AR, extending from the South Pacific across Marie Byrd Land to the Ross Ice Shelf. At its southern tip, a portion of ~~this~~  
642 Wille IWV AR was also classified as an AR-child, indicating sustained, concentrated moisture transport embedded within the  
643 broader IWV and IVT structure. This episode produced exceptionally strong surface temperature anomalies over the Ross Ice  
644 Shelf, locally exceeding +30 °C. On the following day, the anticyclonic anomaly shifted southward toward the South Pole,  
645 while the low-pressure system elongated eastward, forming a double-centered trough. Together, these systems established a  
646 broad zonal corridor that directed the DARK AR across the Antarctic interior. By the third day, the AR extended along the  
647 southern flank of the EAID, maintaining a coherent filament structure. G&W v4 still detects the feature on this day but its  
648 detection stops shortly after the coastline, failing to follow the moisture plume as it propagates inland with DARK. The warm  
649 anomalies migrated with the AR core, indicating active advection of heat and moisture along its path. By the fourth day, the

650 AR weakened and contracted into a diminished AR structure centered near the South Pole and extending over southern  
651 Dronning Maud Land and southern Princess Elizabeth Land. Despite this decay, pronounced 2 m air temperature anomalies  
652 persisted over the region previously covered by the main AR on day 3, rather than beneath the contracted AR-child itself,  
653 reflecting the lingering thermal influence of the moist and warm air mass advected during peak AR activity rather than active  
654 transport at this stage ~~transported deep into the Antarctic interior.~~





656

657 Figure 110. Synoptic evolution of three ~~South Pole-crossing~~-DARK AR events penetrating south of 85° S. Rows (a–c)  
 658 correspond to the events from 30 July–2 August 1991, 11–14 May 2018, and 31 August–3 September 2020, respectively.  
 659 Columns show sequential days at 00 UTC. Filled colors depict 2 m air temperature anomalies (°C), and grey contours show  
 660 500-hPa geopotential-height anomalies (m; solid = positive, dashed = negative) at 50-m intervals. DARK ARs (solid magenta)

661 and their children (dashed magenta) are shown together with Wille ARs (solid blue = vIVT; dashed blue = IWV) and G&W  
662 v4 ARs (limegreen). The dashed circle marks 85° S, and regions north of 60° S are masked.

#### 663 4 Discussion & Conclusion

664 The DARK framework bridges the gap between the intensity-focused Antarctic schemes of Wille vIVT and IWV and the  
665 globally applied IVT-based approaches such as Guan and Waliser (2015, 2019), while extending the geometric flexibility  
666 recently introduced by Spensberger et al. (2025). Building on Wille's methods, DARK retains the strict 98th-percentile  
667 threshold to isolate the most intense moisture-transport events while introducing key advancements: it uses total IVT rather  
668 than only its meridional component and computes total filament length instead of meridional extent, thereby removing the  
669 directional and geometric constraints that previously limited the detection of curved or equatorward-turning ARs. Global IVT-  
670 based schemes such as Guan and Waliser (2015, 2019, 2024) also use IVT magnitude but impose a directional coherence  
671 constraint that may limit the detection of ARs with strongly curved or reversing geometries~~excludes ARs curving or reversing~~  
672 flow direction. By relaxing this requirement, DARK identifies dynamically coherent, non-meridional ARs that are common  
673 near the Antarctic coast, where synoptic steering, Coriolis deflection, and topographic deflection distort moisture pathways.

674 Unlike previous frameworks, DARK eliminates the artificial boundary effects that limited AR detection close to the poles. In  
675 Wille vIVT, the reversal of the meridional IVT component at the South Pole prevents continuous detection of pole-crossing  
676 features, while the 20° meridional extent criterion introduces a secondary edge effect up to about 65° S. The Wille IWV scheme  
677 avoids the vIVT singularity but remains affected by this geometric limitation, because it was developed and applied assuming  
678 a southward boundary at 85°S. G&W v4 avoids these specific boundary issues but introduces a different spatial limitation: its  
679 hemispheric IVT threshold is very permissive along the coast and over West Antarctica, generating far more AR detections  
680 than DARK or the Wille schemes in these regions, while being very restrictive over the cold, dry East Antarctic interior, where  
681 its effective threshold prevents detection of the weaker but climatologically relevant moisture intrusions that DARK and Wille  
682 capture. This results in a highly heterogeneous detection footprint, with overdetection at the coast and underdetection inland,  
683 and only a narrow transitional zone where detection frequencies are broadly comparable to those of DARK or the Wille  
684 schemes. This reflects the fundamental mismatch between a hemispheric IVT threshold and the strong spatial gradients in  
685 Antarctic IVT climatology, making G&W v4 better suited for characterizing coastal AR activity rather than tracking AR  
686 influence across the full Antarctic continent and into the interior. By using total IVT and defining the 2,000 km minimum  
687 extent along the full curved axis of the filament rather than its meridional projection, DARK, together with the AR-children  
688 add-on, enables continuous tracking of ARs throughout their lifecycle, from oceanic genesis across the Antarctic continent and  
689 occasionally the South Pole to their inland decay and fragmentation as AR-children. This provides a seamless representation  
690 of poleward moisture transport and its persistence over the ice sheet.

691 The climatology derived from DARK ARs is broadly consistent with that of Wille vIVT and IWV, confirming that it preserves  
692 the physical realism of established Antarctic AR frameworks. A majority of Wille ARs are detected by DARK, and overall  
693 AR frequency along the Antarctic coast remains similar to that obtained with Wille's schemes, indicating strong agreement to  
694 detect the initial moisture intrusions. This shows that the method extends rather than replaces previous approaches: Wille ARs  
695 represent some of the most intense events, accounting for much of the precipitation and extreme anomalies. DARK additionally  
696 identifies ARs systematically missed by Wille's directional and geometric constraints. These new detections occur mainly  
697 south of the EAID, but additional events are found across the continent wherever moisture plumes turn zonally or overturn  
698 under the combined influence of vorticity and topography. These ARs are dynamically coherent systems associated with strong  
699 precipitation, pronounced temperature anomalies, and compound extremes. Their frequency aligns with the 20 % of  
700 extratropical moisture-transport axes that turn equatorward beyond 70° S (Spensberger et al., 2025), although the proportion  
701 is smaller here (about 6 %), suggesting that the most intense filaments, such as those detected by Wille, are less likely to  
702 overturn than weaker or more diffuse transports. While Wille vIVT remains most effective at isolating direct, intense poleward  
703 intrusions, DARK complements it by capturing a broader spectrum of AR geometries that are still physically meaningful and  
704 climatically relevant.

705 DARK ARs account for an average of 18 % of total Antarctic precipitation, compared to about 13 % in Wille vIVT. The largest  
706 increases occur in coastal embayments and across catchments south of the EAID, where the inclusion of AR-children further  
707 amplifies local contributions, raising them from only a few percent in Wille vIVT to over 20 %. This rise does not result from  
708 more intense precipitation within individual events but from a higher occurrence and greater diversity of ARs detected by  
709 DARK. On average, individual DARK ARs are associated with slightly lower mean precipitation per event than Wille ARs,  
710 which remain the most precipitation-intense. However, DARK also identifies additional ARs that are moderately weaker while  
711 still belonging to the upper tail of the precipitation distribution. In particular, DARK captures a larger fraction of precipitation  
712 extremes, as defined above by the daily 99th-percentile anomaly, with the strongest signals in regions such as McMurdo,  
713 Victoria Land, and near the South Pole south of the EAID. A similar pattern emerges for 2 m air temperature and compound  
714 extremes, where DARK detects more events than Wille. Risk ratio analysis confirms that this stronger association with  
715 extremes is not simply a by-product of higher AR frequency: extreme events are statistically more likely to occur during DARK  
716 ARs than during Wille ARs, and even more so when AR-children are included. The comparison with G&W v4 reveals a  
717 contrasting picture for both precipitation attribution and risk ratios. While G&W v4 explains more total precipitation along the  
718 coast and over West Antarctica due to its high detection frequency in these regions, DARK explains substantially more inland,  
719 particularly north of the EAID where G&W v4 detections drop sharply. For extreme events, the same coastal-to-inland polarity  
720 applies, but the continent-wide mean difference remains positive in favor of DARK, as the abundance of G&W v4 coastal  
721 detections inevitably captures most extreme days by volume while attributing a large share of precipitation to non-extreme  
722 events. The very high RR values of G&W v4 along the coast reflect this detection structure. Conversely, inland where G&W  
723 v4 detections are sparse, the few detected ARs are almost exclusively associated with extreme events, while the vast non-AR

724 pool again drives the denominator toward zero. In both cases, the RR is not physically comparable to that of DARK or the  
725 Wille schemes, which maintain a spatially consistent detection range across the continent. This highlights a general limitation  
726 of the RR metric when comparing ARDTs with strongly contrasting detection frequencies: RR conflates physical association  
727 strength with detection selectivity, and should be interpreted alongside occurrence and fraction of extremes explained when  
728 assessing cross-ARDT performance.

729 Another key contribution of this work lies in the introduction of the AR-children module, which extends detection beyond  
730 landfall by identifying remnants with high moisture transport that remain dynamically connected to their parent ARs. As ARs  
731 encounter the Antarctic coast, condensation, latent heating, and orographic deflection often disrupt their filamentary structure,  
732 causing them to fall below the length or coherence thresholds of conventional algorithms. These fragments, although shorter,  
733 maintain IVT above the 98th percentile and continue to produce significant precipitation and temperature anomalies inland.  
734 The AR-children algorithm captures these post-landfall features, enabling the representation of the decaying yet dynamically  
735 active stages of the ARs (Wille et al., 2024). In Antarctica, AR-children are particularly important over Victoria Land and the  
736 Amery Ice Shelf, where they account for more than 8 % of total precipitation and contribute up to 20 % of all extreme events,  
737 including precipitation, temperature, and compound extremes. When AR-children are included in addition to DARK ARs, the  
738 mean association with precipitation extremes increases from 53 % to 58 %, with temperature extremes from 67 % to 71 %,  
739 and with compound extremes from 80 % to 83 %. These results demonstrate that AR-children are not marginal phenomena  
740 but intrinsic components of the Antarctic AR lifecycle, representing the decaying inland phase of ARs and accounting for their  
741 delayed effects on precipitation and temperature extremes. From a practical standpoint, users whose focus is limited to coastal  
742 AR landfalls and their immediate impacts may find the core DARK algorithm sufficient, given its substantially lower  
743 computational cost, while the AR-children module is recommended for studies focusing on inland moisture transport and  
744 surface impacts.

745 Despite these advances, DARK remains subject to methodological assumptions that introduce uncertainty. A minimum AR  
746 length of 2,000 km was imposed to match the typical scale of ARs described in the literature (e.g., Guan and Waliser, 2015;  
747 Wille et al., 2021; Skinner et al., 2020; Gorodetskaya et al., 2014), generally longer than 2,000 km and narrower than 1,000  
748 km. DARK does not explicitly constrain AR width, as the use of IVT naturally favors elongated structures, in contrast with  
749 IWV-based schemes that can produce broad, static moisture plumes. The AR-children module further applies a minimum  
750 feature area of 20,000 km<sup>2</sup> to remove small, short-lived moisture patches. This threshold is not physically based but chosen  
751 pragmatically to exclude spurious, localized post-landfall features. These thresholds are empirically motivated by case-study  
752 analyses, which show that post-AR moist structures typically extend over at least this spatial scale. While a comprehensive  
753 sensitivity analysis is beyond the scope of this study, future work could further explore how varying these thresholds affects  
754 detection frequency and precipitation attribution. Likewise, the 15-day rolling window used to compute the 98th-percentile  
755 IVT threshold improves upon monthly percentiles by avoiding discontinuities at month boundaries, but it adds complexity that

756 may affect reproducibility. These design choices illustrate the necessary balance between physical robustness and algorithmic  
757 simplicity inherent to percentile-based detection frameworks.

758 As with all threshold-based methods, DARK defines discrete events within a continuous moisture field. The 98th-percentile  
759 threshold represents both an empirical compromise between inclusiveness and selectivity and a deliberate choice to ensure  
760 methodological continuity with previous Antarctic AR frameworks, particularly Wille vIVT and IWV. Lowering the threshold  
761 would inflate detections but weaken dynamical coherence, while raising it would isolate too few, overly intense events.  
762 Retaining the 98th percentile thus preserves comparability with earlier studies while providing a pragmatic balance that isolates  
763 physically meaningful ARs and maintains statistical consistency. Future work could explore adaptive thresholds that evolve  
764 with temperature, such as those proposed by Barthélemy et al. (2025) and Macleannan et al. (2025), to better represent  
765 thermodynamic scaling under warming conditions and to extend the applicability of DARK and related tools across diverse  
766 climate states, from palaeoclimate to future projections.

767 Overall, DARK provides a coherent and physically consistent framework for characterizing Antarctic ARs and their climatic  
768 influence. By removing directional and geometric constraints, eliminating artificial boundaries at the pole, and, with the add-  
769 on incorporating post-landfall detection through AR-children, it allows continuous tracking of ARs from oceanic genesis to  
770 polar dissipation. In doing so, DARK better captures the full lifecycle of Antarctic ARs, from their formation in the lower  
771 latitudes, through landfall and inland decay, including a potential passage across the South Pole, thereby providing an  
772 unprecedentedly complete view of AR-driven moisture and energy transport over the Antarctic Ice Sheet. In addition to further  
773 highlighting the SMB impacts of ARs across the entire Antarctic Ice Sheet as seen here, DARK provides a tool for tracking  
774 the influence of residual AR moisture on Antarctic mesoscale-scale atmospheric dynamics like polar lows and barrier jets  
775 (Carrasco and Bromwich, 1993; Nigro et al., 2012). This framework bridges global and polar perspectives, linking large-scale  
776 moisture transport pathways to regional precipitation, temperature, and compound extremes over the Antarctic Ice Sheet, and  
777 highlighting that the influence of ARs extends well beyond their initial landfall.

#### 778 **Code and data availability**

779 The DARK algorithm was developed in Python and is publicly available under an open-source license at  
780 [https://github.com/victoirebuffet/DARK\\_atmospheric\\_river\\_detection\\_tool](https://github.com/victoirebuffet/DARK_atmospheric_river_detection_tool). The detection and analysis scripts rely on  
781 standard Python libraries including xarray, numpy, scipy, matplotlib, and cartopy, and are designed to process ERA5 reanalysis  
782 data in NetCDF format, however codes were made for MERRA-2 and CESM-LE2, codes are available upon request. ERA5  
783 reanalysis data (Hersbach et al., 2023a; Hersbach et al., 2023b) are available from the Copernicus Climate Data Store (CDS)  
784 at <https://cds.climate.copernicus.eu/>. The DARK AR catalog is available at <https://doi.org/10.5281/zenodo.17963007>, while  
785 the DARK AR+children catalog is available at <https://doi.org/10.5281/zenodo.17962931>. [The AR-children detection module](#)  
786 [requires substantially more computational resources than the core DARK algorithm. Processing the full 1979–2023 ERA5](#)

787 [climatology in a single run requires approximately 9h of CPU time and ~17 GB of memory on a single CPU core, compared](#)  
788 [to 1h and ~8 GB for the core DARK algorithm. Users requiring only AR detection without post-landfall remnant tracking can](#)  
789 [therefore run DARK at negligible computational cost, while the AR-children module is recommended for studies focusing on](#)  
790 [inland moisture transport or the full AR life cycle.](#) AR catalogs for Wille vIVT and Wille IWV, re-run from the method of  
791 Wille et al. (2021), on the full period of study (1979–2023), are available at <https://doi.org/10.5281/zenodo.17968902>.

## 792 **Author contributions**

793 VB developed the detection algorithms, curated and analyzed the data, and prepared the initial draft of the manuscript,  
794 including figures and visualizations. VF and BP guided the investigation, and contributed to refining the final version of the  
795 manuscript. JW contributed to the conceptual development of the study, provided scientific guidance throughout the research  
796 process, and contributed to revising the final manuscript.

## 797 **Competing interests**

798 The authors declare that they have no conflict of interest.

## 799 **Financial support**

800 This research has been supported by the Agence Nationale de la Recherche (ANR) under project ANR-20-CE01-0013  
801 (ARCA).

## 802 **Acknowledgements**

803 We thank the European Centre for Medium-Range Weather Forecasts (ECMWF) for providing the ERA5 reanalysis data. We  
804 thank Juliette Blanchet for valuable feedback on the significance testing. [We thank Bin Guan for kindly providing the G&W](#)  
805 [v4 AR catalogue. We thank the two anonymous reviewers whose constructive comments improved the manuscript.](#) We thank  
806 the developers of python, matplotlib, cartopy, xarray, scipy, numpy, scikit-image, geopy, netcdf4, networkx and pandas.  
807 Calculations were performed using HPC resources from DNUM CCUB (Centre de Calcul de l'Université Bourgogne Europe).

## 808 **References**

809 Adusumilli, S., A. Fish, M., Fricker, H. A., and Medley, B.: Atmospheric River Precipitation Contributed to Rapid Increases  
810 in Surface Height of the West Antarctic Ice Sheet in 2019, *Geophysical Research Letters*, 48, e2020GL091076,  
811 <https://doi.org/10.1029/2020GL091076>, 2021.

812  
813 American Meteorological Society, Glossary of Meteorology: Atmospheric River.  
814 <https://glossary.ametsoc.org/wiki/Atmospheric--river>, 20224.

815  
816 Barthélemy, L., Codron, F., Wille, J., Favier, V., & Clem, K. R.: Future atmospheric rivers in Antarctica: Characteristics and  
817 impacts with the IPSL model. *Journal of Geophysical Research: Atmospheres*, 130, e2025JD043398.  
818 <https://doi.org/10.1029/2025JD043398>, 2025.

819  
820 Carrasco, J. F. and Bromwich, D. H.: Mesoscale cyclogenesis dynamics over the southwestern Ross Sea, Antarctica, *Journal of*  
821 *Geophysical Research: Atmospheres*, 98, 12973–12995, <https://doi.org/10.1029/92JD02821>, 1993.

822  
823 Chang, E. K. M., Lee, S., and Swanson, K. L.: Storm Track Dynamics, *Journal of Climate*, 15, 2163–2183,  
824 [https://doi.org/10.1175/1520-0442\(2002\)015%253C02163:STD%253E2.0.CO;2](https://doi.org/10.1175/1520-0442(2002)015%253C02163:STD%253E2.0.CO;2), 2002.

825  
826 [Chemke, R., Zanna, L., Orbe, C., Sentman, L. T., and Polyani, L. M.: The Future Intensification of the North Atlantic Winter](https://doi.org/10.1175/JCLI-D-21-0407.1)  
827 [Storm Track: The Key Role of Dynamic Ocean Coupling, \*Journal of Climate\*, 35, 2407–2421, \[https://doi.org/10.1175/JCLI-\]\(https://doi.org/10.1175/JCLI-D-21-0407.1\)](https://doi.org/10.1175/JCLI-D-21-0407.1)  
828 [D-21-0407.1., 2022.](https://doi.org/10.1175/JCLI-D-21-0407.1)

829  
830 Collow, A. B. M., Shields, C. A., Guan, B., Kim, S., Lora, J. M., McClenny, E. E., Nardi, K., Payne, A., Reid, K., Shearer, E.  
831 J., Tomé, R., Wille, J. D., Ramos, A. M., Gorodetskaya, I. V., Leung, L. R., O'Brien, T. A., Ralph, F. M., Rutz, J., Ullrich, P.  
832 A., and Wehner, M.: An Overview of ARTMIP's Tier 2 Reanalysis Intercomparison: Uncertainty in the Detection of  
833 Atmospheric Rivers and Their Associated Precipitation, *Journal of Geophysical Research: Atmospheres*, 127,  
834 e2021JD036155, <https://doi.org/10.1029/2021JD036155>, 2022.

835  
836 Dacre, H. F. and Clark, P. A.: A kinematic analysis of extratropical cyclones, warm conveyor belts and atmospheric rivers, *npj*  
837 *Clim Atmos Sci*, 8, 97, <https://doi.org/10.1038/s41612-025-00942-z>, 2025.

838  
839 Gorodetskaya, I. V., Tsukernik, M., Claes, K., Ralph, M. F., Neff, W. D., and Van Lipzig, N. P. M.: The role of atmospheric  
840 rivers in anomalous snow accumulation in East Antarctica, *Geophysical Research Letters*, 41, 6199–6206,  
841 <https://doi.org/10.1002/2014GL060881>, 2014.

842  
843 Gorodetskaya, I. V., Durán-Alarcón, C., González-Herrero, S., Clem, K. R., Zou, X., Rowe, P., Rodriguez Imazio, P., Campos,  
844 D., Leroy-Dos Santos, C., Dutrievoz, N., Wille, J. D., Chykhareva, A., Favier, V., Blanchet, J., Pohl, B., Cordero, R. R., Park,  
845 S.-J., Colwell, S., Lazzara, M. A., Carrasco, J., Gulisano, A. M., Krakovska, S., Ralph, F. M., Dethinne, T., and Picard, G.:  
846 Record-high Antarctic Peninsula temperatures and surface melt in February 2022: a compound event with an intense  
847 atmospheric river, *npj Clim Atmos Sci*, 6, 1–18, <https://doi.org/10.1038/s41612-023-00529-6>, 2023.

848  
849 Guan, B. and Waliser, D. E.: Detection of atmospheric rivers: Evaluation and application of an algorithm for global studies:  
850 Detection of Atmospheric Rivers, *J. Geophys. Res. Atmos.*, 120, 12514–12535, <https://doi.org/10.1002/2015JD024257>, 2015.

851  
852 Guan, B. and Waliser, D. E.: Tracking Atmospheric Rivers Globally: Spatial Distributions and Temporal Evolution of Life  
853 Cycle Characteristics, *Journal of Geophysical Research: Atmospheres*, 124, 12523–12552,  
854 <https://doi.org/10.1029/2019JD031205>, 2019.

855

856 [Guan, B. and Waliser, D. E.: A regionally refined quarter-degree global atmospheric rivers database based on ERA5, \*Scientific\*](https://doi.org/10.1038/s41597-024-03258-4)  
857 [Data, 11, 440, <https://doi.org/10.1038/s41597-024-03258-4>, 2024.](https://doi.org/10.1038/s41597-024-03258-4)

858

859 Hersbach, H., Bell, B., Berrisford, P., Hirahara, S., Horányi, A., Muñoz-Sabater, J., Nicolas, J., Peubey, C., Radu, R., Schepers,  
860 D., Simmons, A., Soci, C., Abdalla, S., Abellan, X., Balsamo, G., Bechtold, P., Biavati, G., Bidlot, J., Bonavita, M., De Chiara,  
861 G., Dahlgren, P., Dee, D., Diamantakis, M., Dragani, R., Flemming, J., Forbes, R., Fuentes, M., Geer, A., Haimberger, L.,  
862 Healy, S., Hogan, R. J., Hólm, E., Janisková, M., Keeley, S., Laloyaux, P., Lopez, P., Lupu, C., Radnoti, G., De Rosnay, P.,  
863 Rozum, I., Vamborg, F., Villaume, S., and Thépaut, J.: The ERA5 global reanalysis, *Quart J Royal Meteor Soc*, 146, 1999–  
864 2049, <https://doi.org/10.1002/qj.3803>, 2020.

865

866 Hersbach, H., Bell, B., Berrisford, P., Biavati, G., Horányi, A., Muñoz Sabater, J., Nicolas, J., Peubey, C., Radu, R., Rozum,  
867 I., Schepers, D., Simmons, A., Soci, C., Dee, D., Thépaut, J.-N.: ERA5 hourly data on pressure levels from 1940 to present.  
868 Copernicus Climate Change Service (C3S) Climate Data Store (CDS), DOI: <https://doi.org/10.24381/cds.bd0915c6>, 2023b.

869

870 Hersbach, H., Bell, B., Berrisford, P., Biavati, G., Horányi, A., Muñoz Sabater, J., Nicolas, J., Peubey, C., Radu, R., Rozum,  
871 I., Schepers, D., Simmons, A., Soci, C., Dee, D., Thépaut, J.-N. : ERA5 hourly data on single levels from 1940 to present.  
872 Copernicus Climate Change Service (C3S) Climate Data Store (CDS) : <https://doi.org/10.24381/cds.adbb2d47>, 2023b.

873

874 Katz, D., Baptista, J., Azen, S. P., and Pike, M. C.: Obtaining Confidence Intervals for the Risk Ratio in Cohort Studies,  
875 *Biometrics*, 34, 469–474, <https://doi.org/10.2307/2530610>, 1978.

876

877 Maclennan, M. L., Lenaerts, J. T. M., Shields, C., and Wille, J. D.: Contribution of Atmospheric Rivers to Antarctic  
878 Precipitation, *Geophysical Research Letters*, 49, e2022GL100585, <https://doi.org/10.1029/2022GL100585>, 2022.

879

880 Maclennan, M. L., Winters, A. C., Shields, C. A., Thaker, R., Barthelemy, L., Codron, F., and Wille, J. D.: Rising atmospheric  
881 moisture escalates the future impact of atmospheric rivers in the Antarctic climate system, *Commun Earth Environ*, 6, 369,  
882 <https://doi.org/10.1038/s43247-025-02333-x>, 2025.

883

884 Mattingly, K. S., Mote, T. L., and Fettweis, X.: Atmospheric River Impacts on Greenland Ice Sheet Surface Mass Balance,  
885 *Journal of Geophysical Research: Atmospheres*, 123, 8538–8560, <https://doi.org/10.1029/2018JD028714>, 2018.

886

887 Nigro, M. A., Cassano, J. J., Lazzara, M. A., and Keller, L. M.: Case Study of a Barrier Wind Corner Jet off the Coast of the  
888 Prince Olav Mountains, Antarctica, *Monthly Weather Review*, 140, 2044–2063, <https://doi.org/10.1175/MWR-D-11-00261.1>,  
889 2012.

890

891 [Scholz, S. R. and Lora, J. M.: Atmospheric rivers cause warm winters and extreme heat events, \*Nature\*, 636, 640–646,](https://doi.org/10.1038/s41586-024-08238-7)  
892 <https://doi.org/10.1038/s41586-024-08238-7>, 2024.

893

894 Skinner, C. B., Lora, J. M., Payne, A. E., and Poulsen, C. J.: Atmospheric river changes shaped mid-latitude hydroclimate  
895 since the mid-Holocene, *Earth and Planetary Science Letters*, 541, 116293, <https://doi.org/10.1016/j.epsl.2020.116293>, 2020.

896

897 Spensberger, C., Konstali, K., and Spengler, T.: Moisture transport axes: a unifying definition for tropical moisture exports,  
898 atmospheric rivers, and warm moist intrusions, *Weather and Climate Dynamics*, 6, 431–446, [https://doi.org/10.5194/wcd-6-](https://doi.org/10.5194/wcd-6-431-2025)  
899 [431-2025](https://doi.org/10.5194/wcd-6-431-2025), 2025.

900

901 Turner, J., Phillips, T., Thamban, M., Rahaman, W., Marshall, G. J., Wille, J. D., Favier, V., Winton, V. H. L., Thomas, E.,  
902 Wang, Z., van den Broeke, M., Hosking, J. S., and Lachlan-Cope, T.: The Dominant Role of Extreme Precipitation Events in  
903 Antarctic Snowfall Variability, *Geophysical Research Letters*, 46, 3502–3511, <https://doi.org/10.1029/2018GL081517>, 2019.

904

905 Wille, J. D., Favier, V., Dufour, A., Gorodetskaya, I. V., Turner, J., Agosta, C., and Codron, F.: West Antarctic surface melt  
906 triggered by atmospheric rivers, *Nat. Geosci.*, 12, 911–916, <https://doi.org/10.1038/s41561-019-0460-1>, 2019.

907

908 Wille, J. D., Favier, V., Gorodetskaya, I. V., Agosta, C., Kittel, C., Beeman, J. C., Jourdain, N. C., Lenaerts, J. T. M., and  
909 Codron, F.: Antarctic Atmospheric River Climatology and Precipitation Impacts, *Journal of Geophysical Research:*  
910 *Atmospheres*, 126, <https://doi.org/10.1029/2020jd033788>, 2021.

911

912 Wille, J. D., Favier, V., Jourdain, N. C., Kittel, C., Turton, J. V., Agosta, C., Gorodetskaya, I. V., Picard, G., Codron, F.,  
913 Santos, C. L.-D., Amory, C., Fettweis, X., Blanchet, J., Jomelli, V., and Berchet, A.: Intense atmospheric rivers can weaken  
914 ice shelf stability at the Antarctic Peninsula, *Commun Earth Environ*, 3, 1–14, <https://doi.org/10.1038/s43247-022-00422-9>,  
915 2022.

916

917 Wille, J. D., Pohl, B., Favier, V., Winters, A. C., Baiman, R., Cavallo, S. M., Leroy-Dos Santos, C., Clem, K., Udy, D. G.,  
918 Vance, T. R., Gorodetskaya, I., Codron, F., and Berchet, A.: Examining Atmospheric River Life Cycles in East Antarctica,  
919 *Journal of Geophysical Research: Atmospheres*, 129, e2023JD039970, <https://doi.org/10.1029/2023JD039970>, 2024.

920

921 Wille, J. D., Favier, V., Gorodetskaya, I. V., Agosta, C., Baiman, R., Barrett, J. E., Barthelemy, L., Boza, B., Bozkurt, D.,  
922 Casado, M., Chyhareva, A., Clem, K. R., Codron, F., Datta, R. T., Durán-Alarcón, C., Francis, D., Hoffman, A. O., Kolbe, M.,  
923 Krakovska, S., Linscott, G., Maclennan, M. L., Mattingly, K. S., Mu, Y., Pohl, B., Santos, C. L.-D., Shields, C. A., Toker, E.,  
924 Winters, A. C., Yin, Z., Zou, X., Zhang, C., and Zhang, Z.: Atmospheric rivers in Antarctica, *Nat Rev Earth Environ*, 6, 178–  
925 192, <https://doi.org/10.1038/s43017-024-00638-7>, 2025.

926

927 Wirth, V., Riemer, M., Chang, E. K. M., and Martius, O.: Rossby Wave Packets on the Midlatitude Waveguide—A Review,  
928 *Monthly Weather Review*, 146, 1965–2001, <https://doi.org/10.1175/MWR-D-16-0483.1>, 2018.

929

930 Zhu, Y. and Newell, R. E.: A Proposed Algorithm for Moisture Fluxes from Atmospheric Rivers, *Monthly Weather Review*,  
931 126, 725–735, [https://doi.org/10.1175/1520-0493\(1998\)126<0725:APAFMF>2.0.CO;2](https://doi.org/10.1175/1520-0493(1998)126<0725:APAFMF>2.0.CO;2)—[https://doi.org/10.1175/1520-](https://doi.org/10.1175/1520-0493(1998)126%253C0725:APAFMF%253E2.0.CO;2)  
932 [0493\(1998\)126%253C0725:APAFMF%253E2.0.CO;2](https://doi.org/10.1175/1520-0493(1998)126%253C0725:APAFMF%253E2.0.CO;2), 1998.

933

934